UNIVERSITY OF HELSINKI REPORT SERIES IN PHYSICS

HU-P-D213

Radiation-induced nanostructure evolution models for Fe alloys

Ville Jansson

Division of Materials Physics
Department of Physics
Faculty of Science
University of Helsinki
Helsingfors, Finland

Academic Dissertation

To be presented, with the permission of the Faculty of Science of the University of Helsinki, for public criticism in auditorium A110 of the Department of Chemistry (Chemicum) on 19th December 2013 at noon.

HELSINGFORS 2013

ISBN 978-952-10-8948-0 (printed version)
ISSN 0356-0961
Helsingfors 2013
Unigrafia

ISBN 978-952-10-8949-7 (PDF version)
http://ethesis.helsinki.fi/
Helsingfors 2013
Electronic Publications @ University of Helsinki

Ville Jansson, **Radiation-induced nanostructure evolution models for Fe alloys**, University of Helsinki, 2013, 68 p. + appendices, Report Series in Physics HU-P-D213, ISSN 0356-0961, ISBN 978-952-10-8948-0 (printed version), ISBN 978-952-10-8949-7 (PDF version)

Abstract

Neutron irradiation induces structural nano-scale changes in steels that in the long term cause degradation of the mechanical properties of the materials. These processes are important to understand to e.g. ensure the integrity of the steel wall of the reactor pressure vessel during the operational life-time of a nuclear power plant. In this thesis, some of the irradiation defects have been studied by using as a model alloy the iron-carbon (Fe-C) system, as iron and carbon are the basic elements in any steel.

The interactions between C and vacancy (V) clusters and between C and self-interstitial atom (SIA) clusters have been studied using Molecular Dynamics simulation techniques. This way C-V clusters, such as C_2V and CV_2, able to trap large SIA clusters, have been identified and characterized. The interaction of SIA clusters, represented by toroidal absorbers, and straight dislocations with point defects, migrating in a 3D or 1D regime, have also been studied by calculating the sink strength, using Object Kinetic Monte Carlo (OKMC). Good agreement with theory is found for both toroidal absorbers and straight dislocations. It is also found that the master curve for the 3D to 1D transition is well reproduced for toroids and fairly well for dislocations. The master curve can thus be said to be valid for any shape of absorbers. It can also be concluded that OKMC takes correctly into account the sink strength of absorbers of any shape.

Using the results from the MD studies of the characterisation of irradiation defects and the latest data collected from other MD, *ab initio*, Atomistic Kinetic Monte Carlo and rate theory studies in the literature, an OKMC model for the irradiation-induced nanostructure evolution in Fe-C has been constructed. The model was validated by reproducing experimental data in terms of vacancy and SIA cluster densities and mean sizes from irradiation experiments at low (340 K) and high operational temperature of light water reactors (560 K), as well as reproducing experimental data from an experiment of post-irradiation annealing up to 700 K. The new model has allowed a deeper understanding of the effect of carbon on the irradiation defect evolution. It was found that the effect of the immobile C-V complexes can be introduced using generic traps for SIA and vacancy clusters. These generic traps have a binding energy that depends on the size of the trapped cluster, which is supported by previously performed atomistic studies. Different trap regimes need to be used at low and high temperatures to account for the different populations of $1/2\langle 111\rangle$ and $\langle 100\rangle$ SIA loops at different temperatures, as

observed in previous TEM studies. The traps are found to have an important function as nucleation points that promote the growth of larger clusters.

The nanostructure evolution model, which is the main result of this thesis, is fully based on physical considerations and only uses a few parameters for calibration. The model is found to be capable of reproducing the experimental trends both at 340 K, 560 K and for annealing up to 700 K; thereby providing insight into the physical mechanisms of importance to determine the type of nanostructural evolution undergone by Fe alloys during irradiation.

Common abbreviations

appm	Atomic parts per million
APT	Atom-Probe Tomography
BWR	Boiling Water Reactor
bcc	Body-centred cubic
C	Carbon
Cu	Copper
DBTT	Ductile-to-brittle transition temperature
dpa	Displacements per atom
Fe	Iron
EAM	Embedded-atom method
fcc	Face-centred cubic
KMC	Kinetic Monte Carlo
LWR	Light Water Reactor
MD	Molecular Dynamics
MMC	Metropolis Monte Carlo
Mn	Manganese
N	Nitrogen
Ni	Nickel
OKMC	Object Kinetic Monte Carlo
PAS	Positron Annihilation Spectroscopy
PWR	Pressurized Water Reactor
RPV	Reactor pressure vessel
RT	Rate Theory
SANS	Small-Angle Neutron Scattering
SIA	Self-interstitial atom
TEM	Transmission Electron Microscope
V	Vacancy
VVER	Vodo-Vodyanoi Energetichesky Reactor

Contents

Chapter 1

Introduction

In 1951, four light bulbs at the National Reactor Testing Station in Idaho were lit by the worlds first electricity generated by nuclear power, using the Experimental Breeder Reactor I (EBR-I), a liquid metal cooled fast reactor [1]. Ever since then, nuclear power has been an important way of generating electricity. In 2010, 428 nuclear power plants existed in 30 countries and they produced about 16 % of the global electrical power supply or 370 GW [2]. In Finland, four nuclear power plants are connected to the grid and they produce 30.6 % of the national electrical power supply (2011) [3]. A fifth reactor is currently under construction in Olkiluoto, which will further increase the nuclear energy supply. Belgium has seven reactors, which produce more than half of the national electricity, and France has 58 reactors, producing 77.7 % of the national electricity (2011) [3], to pick a few examples. Nuclear energy is important in the modern society, as it is dependent on cheap electricity: The total cost of nuclear generated electricity is on average only 0.034 EUR/kWh (2009) [2]. Nuclear energy also has a very low carbon footprint and does not generate any long-lived greenhouse gases, like CO_2 or CH_4, which are believed to be major contributors to the serious environmental issue of the global warming [4].

Nuclear power plants are usually categorized into different generations [5]: To Generation I are counted the prototype reactors built in the 1950s–1970s. Most of them are now decommissioned. Generation II (1970s–1990s) constitutes most reactors that are in use today, including the Boiling Water Reactors (BWR), the Pressurized Water Reactors (PWR), the CANada Deuterium Uranium reactors (CANDU), the Russian reactor designs of Vodo-Vodyanoi Energetichesky Reactor (VVER or sometimes WWER) and Reaktor Bolshoy Moshchnosti Kanalniy (RMBK), and the Advanced Gas-cooled Reactor (AGR). Generation III (1990s–2010) is the current state-of-the-art of nuclear reactor design. This generation has, among other things, improved safety compared to Generation II reactors. The European Pressurized Reactor (EPR), which is the design of the reactor now being built in Olkiluoto,

Finland, belongs to this generation. Other examples are System 80+, AP 600 and Advanced Boiling Water Reactor (ABWR). There are many new reactor designs proposed, which are divided into Generation III+ and Generation IV. Generation III+ has improved efficiency, compared to Generation III, and examples of reactors in this category are AP 1000, Advanced Pressurized Water Reactor (APWR) and Economic Simplified Boiling Water Reactor (ESBWR). In Generation IV are reactor designs that are expected to have lower constructing and operation costs, enhanced safety systems (especially passive safety systems), higher energy production efficiency, resistance to proliferation issues and reduced volumes of radioactive waste. They are expected to be available after 2030 [5]. Fusion reactors are not included in the generations, but a lot of research is currently on-going in this form of nuclear power technology as well. The first prototype reactor large enough to produce excess electricity is currently under construction in Cadarache, France, and planned to be finished 2020 [6]. The advantages with fusion, compared to the fission technologies, are that the fuel materials are deuterium and tritium, which are elements found abundantly in sea water, and the fusion power plants will produce almost no radioactive waste.

Many of the Generation II reactors were built in 1965–1980 and have now reached, or are approaching, the end of the designed life-time, which is normally 40 years. Since it is expensive and sometimes politically difficult to build new nuclear power plants to replace the old ones, the life-time of many Generation II nuclear power plants have been prolonged. In order to do so, the safety and integrity of the reactors have to be ensured. Neutron irradiation during the operation of the nuclear power plant is known to induce nano-scale defects in the steels of the reactor and cause hardening and embrittlement of the materials. Especially the reactor pressure vessel (RPV), that contains the fuel assemblies, is vulnerable to this kind of degradation, as it is extremely hard and expensive to repair or replace. The life-time of the RPV and the rate of the degradation processes in the steel it is made of will thus in effect determine the life-time of the whole power plant.

The degradation of the RPV steels can be assessed by mechanical testing of surveillance capsules, made of the same steels as the RPV and placed nearer to the core of the reactor. The capsules thus endure a higher irradiation flux than the RPV wall and the degradation rate will thus be faster, allowing an estimation of the hardening and embrittlement rate of the RPV walls. The number of surveillance capsules is, however, limited and especially towards the end of the designed life-time of the reactor, other means of ensuring the integrity of the steels have to be adopted.

Deeper understanding of the physical processes driving steel degradation is expected to contribute to define adequate integrity assessment plans beyond the surveillance. Computer simulations have been an essential tool in materials science for more than sixty years. Simulations enable a deeper understanding of the underlying physical processes in materials, that are not always possible to study with experiments. Simulations can thus also contribute to the interpretation of experimental results.

In multi-scale modelling, different computer simulation techniques are used to simulate the processes of the materials on different levels, ranging from the atomic to the macro scale. By using results from high-accuracy small-scale simulations as input to other more approximative, but large-scale, simulations, a multi-scale model can potentially be built to understand macro-phenomena, such as hardening and embrittlement of steels under irradiation. Such a model has to be built step by step, beginning from a thorough understanding of the atomic interactions and the atomic-scale irradiation defects in the materials; followed by an understanding of the nanostructure evolutions, i.e. the change in densities and size distributions of populations of nanometre-sized defect clusters over time, in simple model alloys, such as pure Fe and Fe-C. After that, other elements, such as Cu, Ni and Mn can be added until a complete model for the nanostructure evolution of the RPV steels under irradiation can be constructed. When the nanostructure evolution is known, these results can be used in higher order simulations, such as Dislocation Dynamics and Finite Elements. The final goal is to understand macroscopic changes in mechanical properties of the materials, such as the irradiation-induced hardening and embrittlement of the steels. This is the aim of the European PERFORM60 project of the 7th Euratom Framework Programme [7], which this thesis research project has been a part of.

Chapter 2

Purpose and structure of this study

The purpose of this thesis is to develop a computer model for the radiation-induced nanostructural evolution in Fe-C systems, the base alloy for any steel. The model makes use of the Object Kinetic Monte Carlo (OKMC) simulation method to simulate the long-term (from days to decades of years) evolution of irradiation defects, whose characteristic parameters are obtained by other simulation methods, such as Molecular Dynamics (MD) simulations, which are also used in this thesis. In particular, the interactions between carbon and vacancy clusters and carbon and SIA clusters have been simulated. The results obtained with the model can be used by other simulation techniques, such as Dislocation Dynamics and Finite Element simulations, to estimate the long time scale embrittlement and hardening processes in RPV model alloys and in the long term contribute to the development of a model for the degradation of RPV steels under irradiation.

This thesis contains five papers, of which four are published or accepted for publication in the international peer-reviewed Journal of Nuclear Materials and one is submitted to the same journal. The papers are numbered **I–V** and included after this summary. The structure of this summary is as follows: In this chapter, all publications are shortly presented, as well as the specification of the author's contributions. In Ch. 3 is an overview of reactor pressure vessel steels and irradiation damage in metals in general and in particular in Fe-C. In Ch. 4, the computational methods, MD and OKMC, are presented in detail. Ch. 5 summarizes the work to characterize and parameterize the irradiation defects in Fe-C. In particular, MD studies of the interaction between carbon and vacancy clusters and carbon and self-interstitial atom clusters are discussed, as well as OKMC calculations of the sink strength of dislocations and dislocation loops. In Ch. 6, the OKMC model for the nanostructural evolution under irradiation is presented, followed by the simulation results and applications of the model. Finally, the summary and perspectives of the thesis are given in Ch. 7.

2.1 Summaries of the original publications

Paper I: Interaction of carbon with vacancy and self-interstitial atom clusters in α-iron studied using metallic-covalent interatomic potential, D. Terentyev, N. Anento, A. Serra, V. Jansson, H. Khater and G. Bonny, *Journal of Nuclear Materials* 408 (2011) 271–284.

This work is dedicated to understanding the interaction of carbon-vacancy complexes with glissile dislocation loops, which form in Fe, Fe-based alloys and ferritic steels under irradiation. We apply large scale atomistic simulations coupled with the so-called 'metallic-covalent bonding' interatomic potential for the Fe-C system, known to be the most consistent cohesive model available today. With these techniques we have studied (i) the stability of vacancy-carbon clusters; (ii) the interaction of octahedral carbon with $1/2\langle 111\rangle$ loops; (iii) possibility of the dynamic drag of carbon by $1/2\langle 111\rangle$ loops and (iv) the interaction of $1/2\langle 111\rangle$ loops with the most stable vacancy-carbon clusters expected to occur under irradiation. Finally, we have shown that carbon-vacancy complexes act as strong traps for $1/2\langle 111\rangle$ loops.

Paper II: Sink strength calculations of dislocations and loops using OKMC, V. Jansson, L. Malerba, A. De Backer, C. S. Becquart and C. Domain, *Journal of Nuclear Materials* 442 (2013) 218–226.

The sink strength of dislocations and toroidal absorbers is calculated using Object Kinetic Monte Carlo and compared with the theoretical expressions. We get good agreement for dislocations and loop-shaped absorbers of 3D migrating defects, provided that the volume fraction is low, and fair agreements for dislocations with 1D migrating defects. The master curve for the 3D to 1D transition is well reproduced with loop-shaped absorbers and fairly well with dislocations. We conclude that, on the one hand, the master curve is correct for a wide range of sinks and that, on the other, OKMC techniques inherently take correctly into account the strengths of sinks of any shape, provided that an effective way of appropriately inserting the sinks to be studied can be found.

Paper III: Simulation of the nanostructure evolution under irradiation in Fe-C alloys,
V. Jansson and L. Malerba, *Journal of Nuclear Materials* 443 (2013) 274–285.

The Object Kinetic Monte Carlo technique has proven capable of simulating in a realistic and quantitatively reliable way a whole irradiation process. We have developed a model for simulating Fe-C systems using a physical description of the properties of vacancy and self-interstitial atom (SIA) clusters, based on a selection of the latest data from atomistic studies and other available experimental and theoretical work from the literature. Based on these data, the effect of carbon on radiation defect evolution has been largely understood in terms of formation of immobile complexes with vacancies that in turn act as traps for SIA clusters. It is found that this effect can be introduced using generic traps for SIA and vacancy clusters, with a binding energy that depends on the size of the clusters, also chosen on the basis on previously performed atomistic studies.

The model proved to be suitable to reproduce the results of low ($<$350 K) temperature neutron irradiation experiments, as well as the corresponding post-irradiation annealing up to 700 K, in terms of defect cluster densities and size distribution, when compared to available experimental data from the literature. The use of traps proved to be instrumental for our model.

Paper IV: OKMC simulations of Fe-C systems under irradiation: sensitivity studies V. Jansson and L. Malerba. Submitted to *Journal of Nuclear Materials*.

This paper continues our previous work on a nanostructural evolution model for Fe-C alloys under irradiation, using Object Kinetic Monte Carlo modelling techniques. We here present a number of sensitivity studies of parameters of the model, such as the carbon content in the material, represented by generic traps for point defects, the importance of traps, the size dependence of traps and the effect of the dose rate.

Paper V: The nanostructure evolution in Fe-C systems under irradiation at 560 K V. Jansson, M. Chiapetto and L. Malerba, *Journal of Nuclear Materials* 442 (2013) 341–349.

This work extends our Object Kinetic Monte Carlo model for neutron irradiation-induced nanostructure evolution in Fe-C alloys to consider higher irradiation temperatures. The previous study concentrated on irradiation temperatures $<$ 370 K. Here we study the evolution of vacancy and self-interstitial atom (SIA) cluster populations at the operational temperature ($\sim$560 K) of light water reactors, by simulating specific reference irradiation experiments.

The model had to be adapted to account for the existence of two kinds of SIA clusters, $1/2\langle 111\rangle$ and $\langle 100\rangle$, as observed in electron microscopy examinations of Fe alloys neutron irradiated at the temperatures of technological interest.

The model, which is fully based on physical considerations and only uses a few parameters for calibration, is found to be capable of reproducing the experimental trends, thereby providing insight into the physical mechanisms of importance to determine the type of nanostructural evolution undergone by the material during irradiation.

2.2 Author's contribution

The author set up and carried out all simulations in Paper **III** and **IV**. In Paper **V**, the simulations were supervised by the author and the analysis scripts were written by the author. Paper **III**–**V** were written by the author. In Paper **II**, the author wrote all parts and carried out all simulations, except the parts concerning the dislocations. In Paper **I**, the author set up and carried out the MD calculations of the interaction and dissociation energy of a carbon atom with vacancy clusters and the interaction of carbon with the 7-SIA cluster.

2.3 Other publications by the author

Simulation of cascades in tungsten-helium, N. Juslin, V. Jansson and K. Nordlund, *Philosophical Magazine* 90 (2010) 3581–3589.

Molecular Dynamics study on the the effect of helium (He) on the irradiation damage in tungsten (W) after displacement cascades. It was found that the overall effect of He in interstitial positions was to increase the amount of damage, while He in substitutional positions reduce it, due to the effect He has on the recombination of tungsten interstitials.

Chapter 3

Irradiation damage in Nuclear reactors

Light Water Reactors (LWR) are thermal reactors that use normal water as coolant and neutron moderator, as opposed to heavy water. The fuel is composed of fissile elements, such as uranium or, to a much lesser extent, plutonium. The two most common Generation II types of reactors are Boiling Water Reactors (BWR) and, especially, Pressurized Water Reactors (PWR). Schematic overviews of the basic principle for electricity generation for BWR and PWR are shown in Figs. 3.1 and 3.2, respectively. The main difference between the two reactor types are that PWR use two separate coolant circuits, while BWR only use one.

The central part of an LWR is the reactor pressure vessel (RPV), inside which the fuel assemblies are placed, forming the core of the reactor, and where the fission reactions take place, as shown in Fig. 3.3. The integrity of the steel wall of the RPV is of paramount importance for safety reasons, as it is the most important barrier to contain the radioactive material. Surrounding the RPV is still an outer containment structure as the last physical barrier of safety. The RPV is usually cylindrical in shape, made of low alloy bainitic steel. Internally, the surface is cladded with about 5 mm layer of austenitic stainless steel, such as Type 308/309, for corrosion protection. Typical dimensions of a RPV are 430 tonnes in weight, 12 m in height and an inner diameter of 4.4 m with a wall thickness at the core belt

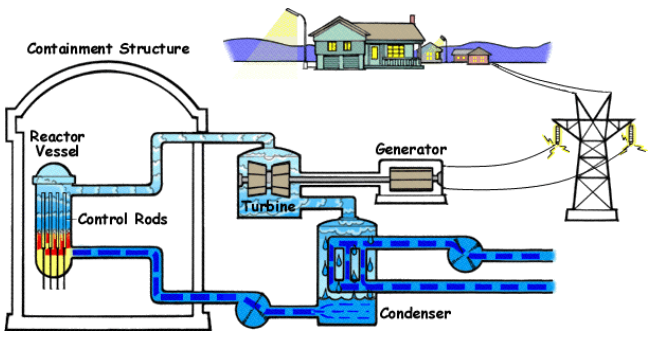

Figure 3.1: Schematic overview of the BWR [8].

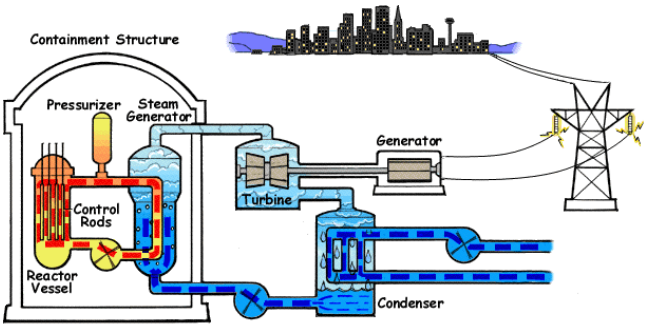

Figure 3.2: Schematic overview of the PWR [9].

line region of 180–250 mm. At the top of the RPV are coolant inlet and outlet nozzles with diameters of about 1.5 m [10].

The scale of the RPV can better be seen in Fig. 3.4, that shows the RPV of the American Shippingport Atomic Power Station in Beaver County, PA, during transportation in 1956. The large size of the RPV means that it is nearly impossible or economically unfeasible to replace it and subsequently the lifetime of the RPV will determine the lifetime of the nuclear power plant. Due to the neutron irradiation, about 0.1 displacements per atom (dpa) are accumulated in the vessel during 40 years of operation, leading to embrittlement and hardening of the steel wall of the RPV. In a worst case scenario, loss of coolant, while under significant pressure, will induce large thermal stresses in the material with cracking and catastrophic failure as a possible outcome. The risk is especially high if the steel is cooled under the ductile-to-brittle transition temperature (DBTT). A good understanding of the embrittlement processes of the RPV steel under irradiation and the temperature at which brittle fracture may occur is thus of utmost importance.

The degradation of the RPV steels are monitored by the use of surveillance capsules of steels identical to those used for the construction of the vessel (base and weld material). The capsules are mounted nearer to the core and thus will endure a higher neutron irradiation flux. Typically, a capsule will accumulate after 10 years as much fluence as the wall will accumulate during 30 years of operation. The capsules are periodically tested for tensile strength, ductility, Charpy notched bar, tensile “dog-bone, and fracture mechanical properties. This way the rate of degradation of the actual RPV wall can be estimated [10]. However, the number of capsules is limited and therefore the number of possible tests are limited too. In particular, the availability of capsules for tests beyond the original designed lifetime of the reactor is limited so that there is a lack of data for extrapolation to high dose ($\sim$0.2 dpa). It is in this context that the development of physical models, such as applying a multi-scale modelling approach, becomes of interest [13].

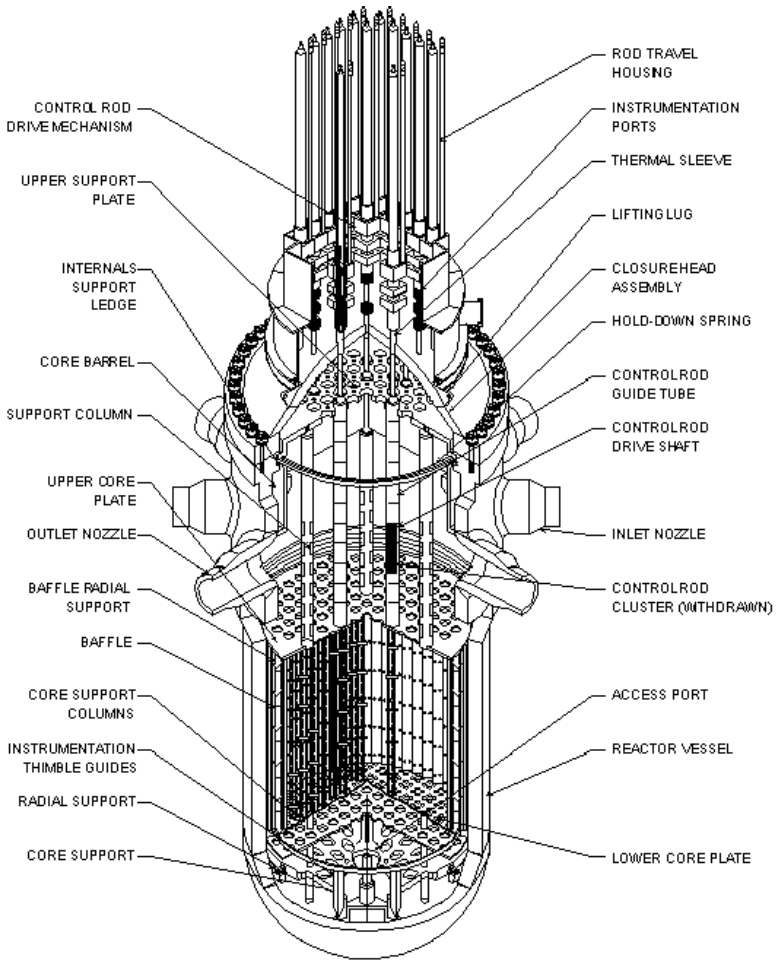

Figure 3.3: Schematic overview of the RPV and the core [11].

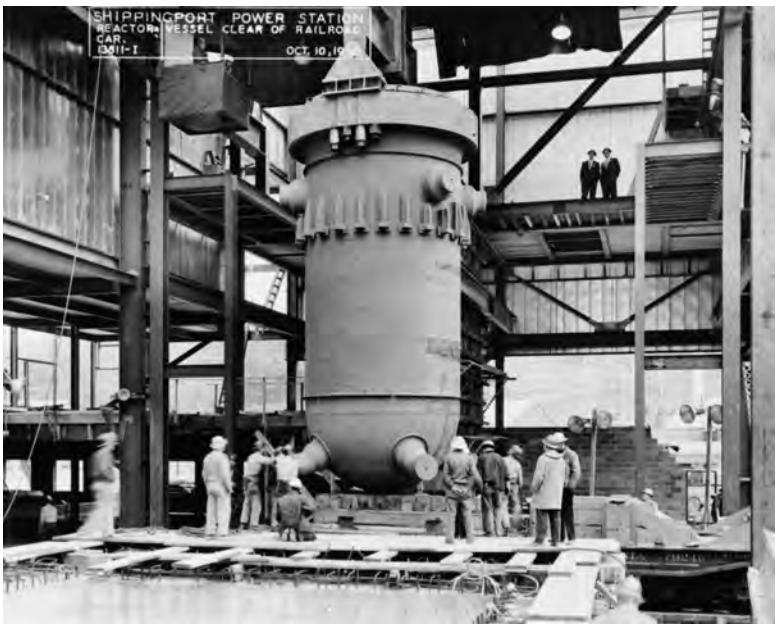

Figure 3.4: The RPV of the Shippingport Atomic Power Station, PA, USA, during transportation in 1956 [12].

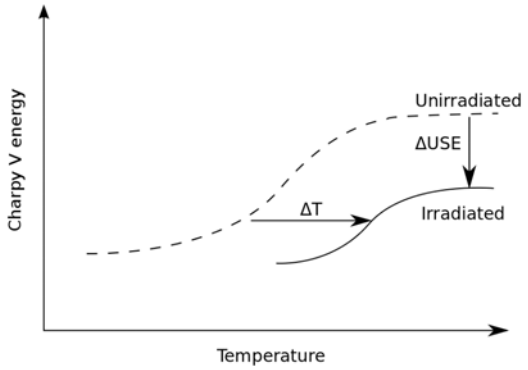

Figure 3.5: Schematic diagram showing the Charpy V notch impact toughness as a function of temperature for unirradiated and irradiated steels and the change of the upper shelf energy (USE) due to irradiation.

3.1 RPV steels

The RPV is made of ferritic-bainitic low alloy steels with bcc structure. The most common steels used in western nuclear power plants are manganese-molybdenum-nickel (MnMoNi) steels, similar to the ASTM A533B1 or ASTM A508-3 specifications. Another alternative is the manganese-molybdenum-chromium (MnMoCr) steel A508-2. In Germany, 22NiMoCr37 or 20MnMoNi55 steels are used and in France 16MnD5. In USA, steels such as SA-533 Grade B: Class 1, SA-508: Grade 2 are used [10, 14]. Eastern designs, such as VVER-440 and VVER-1000, use chromium-molybdenum-vanadium (CrMoV) steels under the specification 15Ch2MFA. Iron (Fe) and carbon (C) are the most important elements as they are the base element in any steel and therefore also in RPV steels. Other important elements are copper (Cu), phosphorus (P), nickel (Ni), silicon (Si) and manganese (Mn). For an overview of the chemical composition of different RPV steels, see [14]. In the initial microstructure of the RPV steels, ferritic, tempered martensitic or bainitic microstructures are usually found: cementite (Fe_3C), Mo_2C, $M_{23}C_6$, M_7C_3, V(CN) and other carbides or carbo-nitrides, depending on the alloy type and heat treatment of the steel [15].

The RPV steels initially have high fracture toughness. However, irradiation during power plant operation leads to increased tensile strength or hardening and reduction in ductility. Irradiated RPV steels have the impact energy curve shifted to higher temperatures and the upper shelf energy is lowered when the impact toughness is measured in a Charpy V test (see Fig. 3.5). Also the DBTT is raised due to neutron irradiation; a phenomenon known as radiation embrittlement [14]. Hardening will also result in a change of the tensile properties, as can be seen in a stress-strain diagram (Fig. 3.6), where the yield stress and ultimate tensile strength are increased with increased neutron fluence.

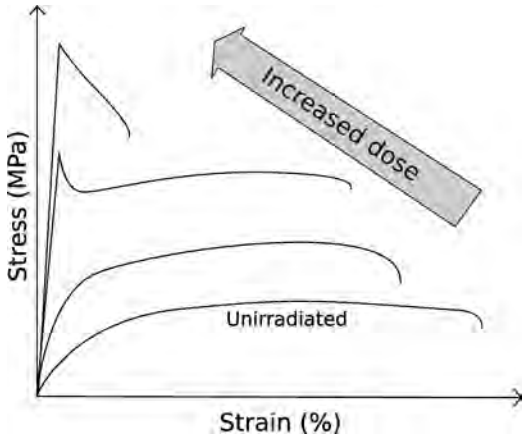

Figure 3.6: Schematic diagram showing the effect of increased neutron dose on the tensile stress-strain curve for typical RPV steels.

The most important factors for embrittlement and hardening are the neutron field (neutron flux, fluence and energy spectrum); the irradiation temperature; impurities, such as Cu and P; and alloying elements, such as Ni and Mn. The most important factor of the neutron field is the neutron fluence, where already a fluence of 10^{22} m^{-2} ($E > 1$ MeV) has an influence on the hardening and embrittlement. The temperature is important as irradiation damage is a thermally activated process: It depends on atomic processes, such as diffusion, recombination, annihilation and segregation of defects, that all strongly depend on the temperature. Generally, higher temperature gives less irradiation damage and significantly so in the 150–400 °C (423–673 K) range. The operation temperature in a LWR is usually somewhat less than 300 °C (573 K) [16]. Cu, Ni and P have been shown to enhance irradiation embrittlement significantly, which is why these elements have been restricted to below 0.1 wt% for Cu and 0.020 wt% for P in RPV steels. Ni is restricted in VVER-1000 reactors to below 1.5 wt% [17].

Irradiation produces point defects such as self-interstitial atoms (SIA) and vacancies, that can form clusters. These point defects make nano-scale changes in the alloy's matrix that leads to hardening [18]. Embrittlement without hardening is also possible as the point defects enhance the diffusion of solute atoms, such as phosphorus, which will go to grain boundaries and change the local chemistry, thereby reducing grain cohesion. This phenomenon is called radiation induced segregation (RIS) and can change material properties, such as the strength or oxidation resistance [14, 19, 20]. Non-hardening embrittlement is measurable by Charpy or fracture mechanical tests.

Solutes can also form defects called precipitates under radiation. These precipitates can be divided into three categories: copper-rich precipitates, manganese-nickel-rich precipitates or so called "late-blooming phases". These clusters of solutes can be more than 1 nm in diameter. They are difficult to observe in Transmission Electron Microscopy measurements (TEM), but other experimental techniques, such as Small-Angle Neutron Scattering (SANS) and Atom-Probe Tomography (APT)

are able to identify them very clearly. The precipitates are able to pin dislocations and thus hinder their movement. The decreased mobility of dislocations leads to increased yield strength and matrix hardening, measurable by hardness tests.

The effect of irradiation hardness and embrittlement in the RPV steels can be mitigated by thermal annealing [10]. By heating the steel using e.g. electrical heating elements and hold it for 150 h and then slowly cool it again, the neutron-induced nanostructural damage will decrease and the copper-rich precipitates will grow so large that they are less effective in blocking the dislocations. Thermal annealing will thus reduce the neutron irradiation induced tensile yield stress and hardness increases and at the same time increase the fracture toughness and ductility of the material. However, such a procedure is not easily realized if not foreseen when the plant is designed. While VVERs are equipped for this annealing, PWRs are generally not.

3.2 Radiation damage in metals

Irradiation damage is caused mainly by energetic neutrons (>1 MeV) that collide with atoms in the material and interact with their nuclei. The interaction times are less than a femtosecond (10^{-15} s). The irradiation effect can be divided into three main outcomes: activation, transmutation and atomic displacement [13, 21, 22]. Activation makes a previously stable atom unstable and radioactive by the absorption of a neutron in the nucleus by inelastic interaction. With transmutation, new chemical elements are created by either absorption of a neutron or emission of a particle from the nucleus, thereby changing the atomic number of the latter. This way extracted protons form hydrogen (H) and alpha particles form helium (He) impurities. Atomic displacements occur when the neutron interacts elastically with an atom, displacing it from its lattice position and forming an interstitial atom and a vacancy. Atomic displacement is the most important irradiation damage mechanism concerning the degradation of RPV steels.

The atom first hit by a neutron is called the primary-knock-on atom (PKA) and it typically starts a chain reaction where a number of other atoms also are displaced, forming a large cascade with a number of sub-cascades, as shown in Fig. 3.7 and Fig. 3.8 [23–26]. Some of the energy of the recoiling atom is lost inducing electronic excitation in the material, but if the energy transferred from the neutron to the atom after the collision is higher than the threshold energy for displacement, E_D, energy is also transferred via elastic and inelastic collisions with other atoms [22, 27, 28]. The deposited energy, excluding the part lost due to electronic excitations, is called damage energy, E_D, as it may, if high enough, cause displaced atoms to displace other atoms and therefore damage the crystal. The overall lifetime of a displacement cascade is only in the order of a few picoseconds (10^{-12} s) and

the affected region is only about ten nanometres ($\sim 10^{-8}$ m) in diameter [13]. After the cascade, stable cascade debris in the form of vacancies (empty lattice sites) and self-interstitial atoms (SIA; off-lattice atoms) or clusters of these are left in the material. These defects will have an impact on the macroscopic properties of the material [13, 19, 29–36]. The total damage, measured as displacements per atoms (dpa), is calculated according to the NRT standard (see Sec. 4.2 and Eq. (4.11)). In this work, results from MD cascade simulations with a damage energy ranging from 5 keV to 100 keV have been used (See e.g. Paper **III**). The RPV wall accumulates about 0.1 dpa during 40 years of operation.

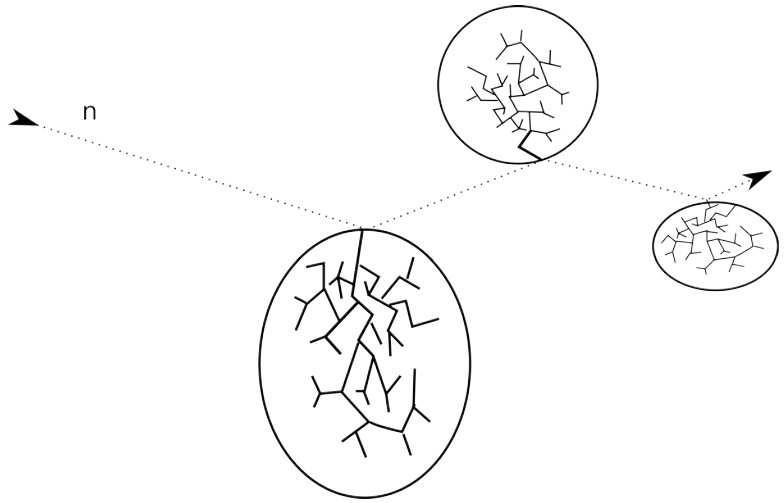

Figure 3.7: Schematic representation of the structure of a cascade.

Both vacancy and SIA defects can migrate, but SIA defects generally migrate faster than vacancy defects [31, 33]. Both defects may disappear at so-called sinks, which may be dislocations, grain boundaries or free surfaces, but vacancies and SIA defects are also sinks for each other, as they will annihilate when they interact [29, 38]. If two defects of the same kind interact with each other, they will cluster. Vacancy clusters usually take a roughly spherical form and become less mobile with increased size. If they grow large enough, they will become voids, visible in TEM. Small voids and even single vacancies are detectable in pure iron and model alloys for RPV using Positron Annihilation Spectroscopy (PAS); small voids are also detected by Small-Angle Neutron Scattering (SANS) [39–41].

SIA clusters form platelets that may have different configurations and different mobilities. TEM studies have observed SIA loops with two kinds of Burgers vectors, $1/2\langle 111\rangle$ and $\langle 100\rangle$ (see Fig. 3.9), in neutron-irradiated pure iron [42–44] and model alloys for RPV steels [45, 46]. $1/2\langle 111\rangle$ loops have been observed in both experiments and in MD simulations to migrate in one dimension and are said to be glissile. If they grow large enough, they will appear like dislocation loops in TEM. Small SIA

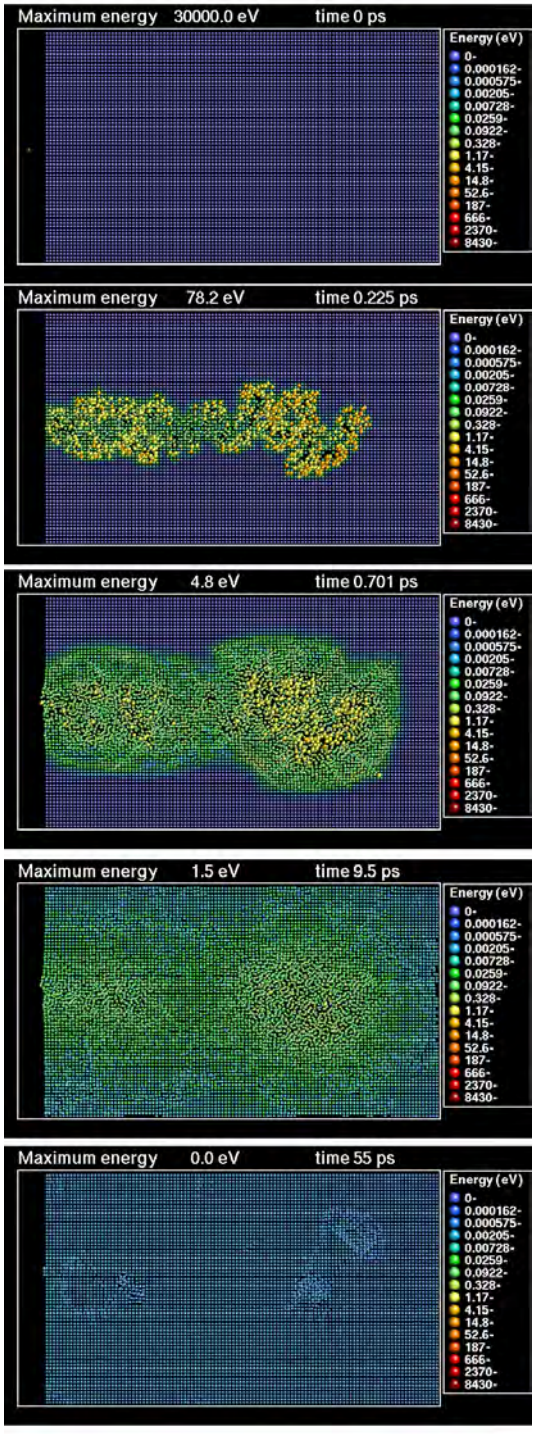

Figure 3.8: MD simulation of a displacement cascade produced by a 30 keV Xe ion on Au. A cross-section of the three-dimensional simulation box is shown at different points in time during the cascade. The temperature of the atoms, represented by spheres, are given by the colour scale. In the end, irradiation defects in the form of point defects and dislocation loops are created. [37]

clusters are not detectable experimentally, but have been simulated with MD (See e.g. [47–51]). The mobility of $\langle 100 \rangle$ loops is still debated, but it is at least a lot less than for $1/2\langle 111 \rangle$ loops [47, 50]. Whereas $1/2\langle 111 \rangle$ loops have been observed to be created in cascades in MD simulations [52–54], the origin of the $\langle 100 \rangle$ loops is also still under debate. Mechanisms for the creation of $\langle 100 \rangle$ loops by interactions between two $1/2\langle 111 \rangle$ loops have been proposed by MD and self-evolving Atomistic Kinetic Monte Carlo (AKMC) studies [55, 56]. Neither loops nor voids are generally observed in irradiated RPV steels, at least at operation conditions; most likely this happens because they do not grow large enough to be detectable [13, 19, 39–41]. Both $1/2\langle 111 \rangle$ and $\langle 100 \rangle$ loops are however commonly observed in other ferritic alloys, such as high-chromium ferritic/martensitic steels and other Fe-Cr alloys [13, 50, 51, 57, 58].

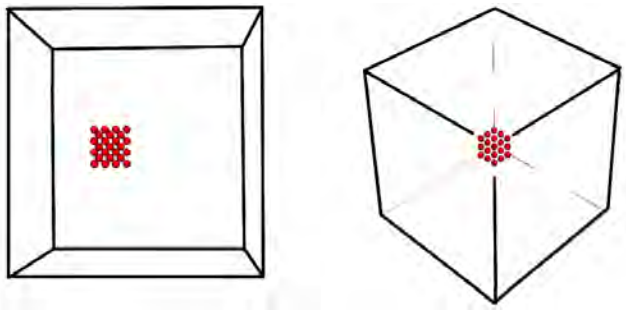

Figure 3.9: A $\langle 100 \rangle$ SIA cluster with 25 SIA (left) and a $1/2\langle 111 \rangle$ SIA cluster with 19 SIA (right), as seen in MD simulations. The SIAs (red) form a platelet cluster in the plane perpendicular to the Burgers vector of the SIA dumbbells.

Copper-rich precipitates are common defects in irradiated RPV steels, as revealed by TEM, SANS and Atom-Probe Tomography (APT). Copper is a common element in RPV steels and almost insoluble in iron, which is why precipitates are easily formed. Other elements like phosphorus, nickel, manganese and silicon are also found in these precipitates, as well as in non-copper precipitates at high doses ($>$0.1 dpa) in other alloys with low or no copper content [41, 59–65].

In austenitic steels, the dominant nanostructural defect is the Frank dislocation loop. This loop is made up of SIAs oriented in a faulted configuration, making the loop sessile. The loops can only migrate after unfaulting [66]. Finally, in pure face-centred cubic (fcc) metals and austenitic steels, stacking-fault-tetrahedra defects have also been observed [67–71].

3.3 Knowledge on irradiation damage in Fe-C

Iron and carbon are the most important elements in steels. In order to understand the nanostructural evolution in any steel under irradiation, the Fe-C system needs to be properly understood first. Since

the 1960s, a relatively large number of irradiation experiments on Fe-C materials have been performed, but few experiments report data with a completeness that would make them useful for the development of an OKMC model. Due to computational restrictions on the OKMC technique, as well as in terms of relevance for the problem of RPV steel embrittlement, only experiments with neutron irradiation with a dose less than 1 dpa are of interest.

The available experiments of interest can be divided into four groups: Irradiation at below 370 K with subsequent annealing [42, 72], irradiation below 370 K (with no subsequent annealing) [44, 73–77], irradiation in a range of different temperatures [78, 79], and irradiation at the operation temperature of the RPV (∼570 K) [39–41, 43, 45, 46, 80–86]. These experiments do not only differ from each other in terms of temperature, but usually also in chemical composition, which is not always reported with the exactness needed for development of a nanostructural model. The material is usually reported as ”iron“ or ”pure iron“, but this rarely means that the material would be completely clean of other elements, like C, N, H and O, which together in some experiment were reported to be of the order of 0.1 weight per cent (wt%). The cumulative content of substitutional impurities were in some cases as high as 0.5 wt%. A detailed review of these experiments can be found in [87].

In order to be able to verify a nanostructural evolution model, the experiments with the most complete data sets for different dose and different temperatures in ranges that are feasible to simulate using OKMC had to be singled out. For low temperature, the experiments by S. J. Zinkle, B. N. Singh, M. Eldrup *et al.* [44, 76] provide data for ”pure iron”, with about 2 weight parts per million (wt. ppm) N and 15 wt. ppm C (about 80 atomic parts per million (appm) together), irradiated at 343 K to 0.23 dpa with TEM and PAS studies to reveal the nanostructural evolution for both vacancies and SIA clusters for different dose. B. L. Eyre and A. F. Bartlett [42] used iron irradiated at 333 K to 0.78 dpa that they annealed up to ∼770 K. The evolution of the SIA clusters were studied using TEM. Finally, the REVE campaign [39–41, 46, 83–86] provides data on Fe-C material irradiated at ∼560 K up to 0.19 dpa with PAS, SANS, APT and TEM studies of the nanostructural evolution at different doses. The C content is estimated to be less than 20 wt. ppm. (about 134 appm).

OKMC is able to simulate nanostructural evolution in terms of defect number density and size distributions, which can be compared directly with experimental data. Single vacancies and vacancy clusters are detectable by PAS and the number density of vacancy defects can thus be measured. PAS, however, does not distinguish between vacancy cluster sizes larger than about 50. SANS and TEM can only resolve vacancy clusters larger than size ∼50 (around 1 nm in diameter). These three techniques can thus together give a quite complete picture of the vacancies in the material.

The other important type of defect in Fe-C materials is the SIA cluster that becomes a dislocation loop at sizes visible in the TEM (around 1–2 nm in diameter). PAS and SANS can not detect SIA

defects, therefore TEM is the only option. SIA clusters smaller than the TEM resolution are thus not experimentally detectable. For the visible SIA clusters, both the number density, the size distribution and the Burgers vectors are normally reported. For iron materials irradiated at $<$370 K, the glissile $1/2\langle 111\rangle$ SIA loops are dominating [44, 73–77], which will grow but keep their Burgers vector if annealed even up to 700 K [42, 72]. In iron, if irradiated at 550–600 K, however, the sessile $\langle 100\rangle$ SIA loops are dominating [41, 45, 46, 80–83].

The migration of $1/2\langle 111\rangle$ SIA loops have been studied both by TEM and in MD simulations. TEM show the loops to go in a fast back and forth motion in one dimension along the closed packed direction of iron and its alloys [49, 88, 89] and the same has been observed in MD simulations, as well [47, 48, 90]. However, in experiments the movements appear to be occasionally stopped by obstacles, too small to be observed in TEM [88]. Arakawa *et al.* [49] also estimated the migration energy of the $1/2\langle 111\rangle$ SIA loops to be $\sim$1.3 eV, which is much higher than the value of 0.05 eV, given by MD simulations. The higher experimental migration energy suggested that the SIA loops are slowed down by invisible obstacles. This hypothesis was furthermore supported by OKMC simulations [91–94], that estimated that some kind of traps with a binding energy of $\sim$1 eV or higher to the SIA loops are needed to prevent all SIA defects to disappear to sinks, such as grain boundaries, in order to have agreement of the model with experiments. The nature of these SIA traps was still an open question four years ago, but proposed candidates were C atoms, vacancy clusters, and C-V complexes, as will be discussed in Ch. 5 and is also the topic of Paper **I**.

Chapter 4

Methods

Computer simulations are sometimes categorised as something between a theoretical and an experimental method. Whereas a simulation method might be based on first-principles physics, which is the case in Density Functional Theory (DFT) or *ab inito* calculations [95], usually considerable approximations are used, which means that the models need to be verified by other means, such as experiments or theoretical calculations. Computer simulations are usually faster and cheaper than doing the real experiments, that in nuclear materials science can take years to perform, and can thus make predictions to help decide which experiments are worth performing. Simulations are also able to give a more detailed picture of what is happening, e.g. on the atomic level that is often hard, if not impossible, to observe in experiments.

Ab initio calculations are based on first-principles physics and thus often provide quite accurate values of properties of atomic systems. The high accuracy, however, poses heavy restrictions on the size of the simulated system ($\sim 10^2$ atoms), as the calculations become very expensive in therms of CPU-time. To speed up the computing time and allow larger systems to be considered, more approximate methods, such as e.g. classical Molecular Dynamics (MD), need to be used. The exactness is decreased, but larger systems and longer time scales can be studied. Since these less accurate methods are no longer based on exact physical laws and thus no longer purely theoretical deductions from fundamental principles and equations, the results need to be verified by experiments. It is, however, not always possible to do experiments to reproduce MD results, because of differences in scales and resolutions. In that case, the results from MD simulations might be used as input to holistic higher order simulations, such as Object Kinetic Monte Carlo (OKMC), Atomistic Kinetic Monte Carlo, Dislocations Dynamics or Finite Elements, to eventually be verified by experiments. In multi-scale modelling a chain of such simulation techniques are thus constructed from highly accurate *ab initio* calculations at small time and spatial scales to higher order and more approximated simulation techniques at larger scales, until the whole chain of models can be completely verified by experiments.

In this thesis, the two different simulation techniques of MD and OKMC have been used. They will be described more in detail in the two following sections.

4.1 Molecular dynamics

Molecular Dynamics was introduced by B. E. Alder and T. E. Wainwright in 1957 [96] and a few years later independently by A. Rahman [97]. It is a simulation method that considers the movements and interactions of atoms or molecules or any system of roughly spherical objects such as e.g. atoms or planets by solving Newton's equations of motion. The forces between the particles need to be given in the form of an inter-particle potential. On the nano-scale, which is the relevant scale for this thesis, systems of up to 10^9 atoms can be simulated with MD.

The general MD algorithm is described in Fig. 4.1. The first step is to give all N atoms initial positions $\mathbf{r}_i$ and velocities $\mathbf{v}_i$. The positions are normally given according to the crystallographic lattice of the material, such as body-centred cubic (bcc) or face-centred cubic (fcc). The velocities are randomly distributed to the atoms according to the Maxwell-Boltzmann distribution and the given initial temperature of the system. In the second step all forces $\mathbf{f}_i(\mathbf{r}_i)$ are calculated.

In the third step the new positions, $\mathbf{r}_i(t_{n+1})$, and velocities $\mathbf{v}(t_{n+1})$ are calculated for an incremental increase of time, t, by a time step Δt, and by solving Newton's equations of motion. The equations of motion for a system with N atoms may be solved using the Lagrangian or the Hamiltonian formalism. The Lagrangian general equation of motion is [98]

$$\frac{d}{dt}\left(\frac{\partial L}{\partial \dot{q}_i}\right) - \frac{\partial L}{\partial q_i} = 0, \tag{4.1}$$

were q_i is the generalized coordinate of atom i, $\dot{q} = \frac{dq}{dt}$ and

$$L(\mathbf{q}, \dot{\mathbf{q}}) = K(\mathbf{q}, \dot{\mathbf{q}}) - V(\mathbf{q}, \dot{\mathbf{q}}) \tag{4.2}$$

is the Lagrangian function, that is the difference between the kinetic energy, K, and the potential energy V. Using Cartesian coordinates, we get that

$$q_i = r_i, \tag{4.3}$$

$$K(\mathbf{r}) = \sum_i^N \frac{1}{2} m_i \dot{r}_i^2, \tag{4.4}$$

$$V = V(\mathbf{r}) \tag{4.5}$$

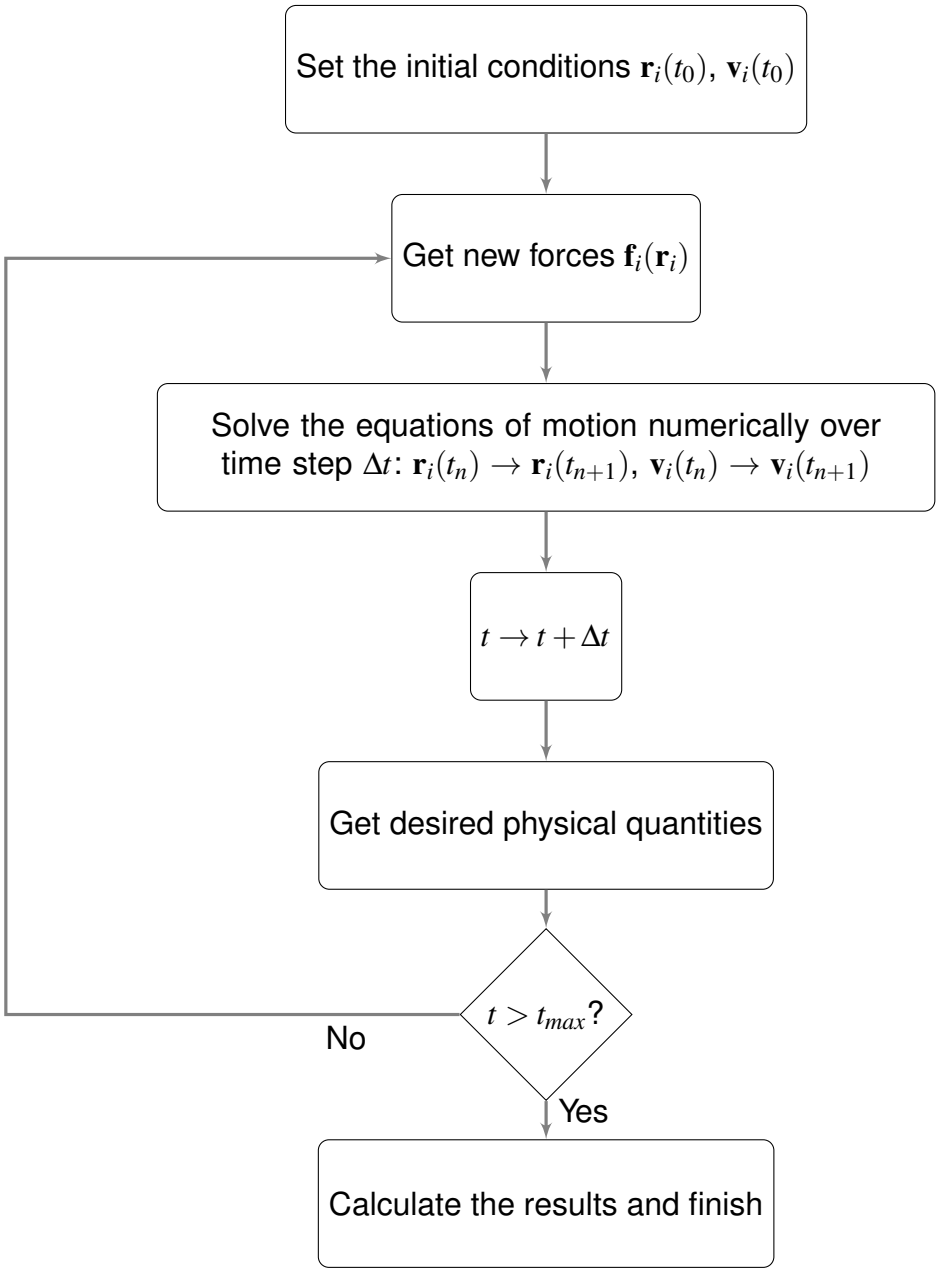

Figure 4.1: The outline of the MD algorithm.

and the resulting equations of motion become

$$m_i \ddot{\mathbf{r}}_i = \nabla_{\mathbf{r}_i} L = -\nabla_{\mathbf{r}_i} V(\mathbf{r}_i) = \mathbf{f}_i \tag{4.6}$$

where $\mathbf{f}_i$ is the force acting on atom i and $V(\mathbf{r}_i)$ is the interatomic potential.

The Lagrangian or Newtonian formalism thus gives a system of $3N$ equations of 2nd order ordinary differential equations, that may be solved e.g. using the Verlet-Størmer algorithm [99, 100].

The time step, Δt, is usually constant throughout the simulation and needs to be chosen small enough to keep the energy conserved in the system. A normal value of the time step is 1–4 fs. A smaller time step makes the simulation more accurate, but increases the duration of the simulation. It is needed only to treat cases of fast atomic motion, such as in the case of the first phases of displacement cascades.

After the time, t, is increased with the time step, Δt, the desired physical quantities of the system are evaluated, such as the temperature, the number of clusters and their energetic properties, or, depending on the statistical ensemble used in the simulation, the total energy or pressure of the system.

The algorithm described above refers to the simulation of a NVE system, a microcanonical ensemble, where the number of atoms, N, the volume, V, and the energy, E, are conserved. This is the simplest ensemble to simulate. For systems where the energy is not conserved, as in e.g. cascade simulations, other ensembles are used, such as NPT (isothermal-isobaric), where P is the pressure; NVT (canonical ensemble) or μVT (grand canonical ensemble), where the chemical potential, μ, is conserved. To obtain average values like the temperature and the total energy, the statistical average of the ensemble is assumed to equal the time averages of the system, according to the ergodic hypothesis [101].

The simulation cycle is repeated step two to six until the maximum time $t = t_{max}$ has been reached, at which point the simulation stops.

The main constraints of the MD method is the availability of CPU-time. Effectively, atomic systems are restricted to be of a few tens of million atoms at most, as the CPU-time increases as $O(N^2)$. Using a cut-off of the inter-atomic interaction ranges, it can be reduced to $O(N)$. Simulated times above $t = 100$ ns are also hard to reach. The constraint on the system size is partly overcome by using periodic boundary conditions, where the simulation box is mirrored in x, y and z direction, to simulate bulk material (of infinite amount). The simulation box still needs to be large enough to avoid boundary artefacts, such as e.g. an atomic cluster interacting with its own mirror image. Finally, the MD method is dependent on the availability of reliable interatomic potentials to correctly simulate a particular system.

4.1.1 Interatomic potentials

The central step of the MD algorithm is to solve Newton's equations of motion, Eq. (4.6). These equations assume the nuclei to be point-like classical particles. The electrons are assumed to be so rapid and light-weight compared to the nuclei, that their explicit motion can be disregarded using the Born-Oppenheimer approximation [102]. This approach of using classical dynamics, instead of the more accurate approach of quantum mechanics, is to a degree corrected by the interatomic potentials that describe all the forces between the atoms based on the ground state of the electronic system. These potentials are either based on experimental or theoretical *ab initio* data or more often a mixture of the two. The quantum mechanical effects will thus be included in the over-all description of the system that the potential provides.

A classical potential can be written as

$$V = \sum_i V_1(\mathbf{r}_i) + \sum_{i,j} V_2(\mathbf{r_i}, \mathbf{r}_j) + \sum_{i,j,k} V_3(\mathbf{r_i}, \mathbf{r}_j, \mathbf{r_k}) + \dots \tag{4.7}$$

where V is the total interatomic potential, V_1 is the single particle potential that considers external forces on particle i, V_2 is the pair potential between two atoms i and j, and V_3 the three-body potential, that might have angular dependencies. Higher order terms, such as four- and five-body potentials are sometimes used for chemical and biological applications. The simplest potentials only consider the two first terms. V_3 is included in some potentials for increased accuracy, but it will also make the computations longer. V_2 and V_3 are enough to describe the basic mechanical and structural properties of most elements and simple compounds.

The only pairwise potential used in this work is the Fe-C potential by R. A. Johnson *et al.* [103] (See Paper **I**). The Fe-Fe part is from [104] and then modified in [103] to allow for impurities of C and N. The two-body central force is designed to match the elastic modulus: sharply repulsive at close separation and goes to zero halfway between the second and third neighbouring atoms. The potential is fitted to reproduce the C migration energy, the experimental activation volume, defined as the difference in volume between a crystal in an energetically stable configuration and in a saddle point configuration, experimentally measured to be essentially zero [105–107]; and the binding energy between a C atom and a vacancy. The migration path for the carbon atom is the straight line from one octahedral point to another with the tetrahedral position as the saddle point. The potential approximates the experimental value of the energy of a C in solution in Fe relative to Fe_3C and gives the correct relaxation strength for internal friction, but does not correctly reproduce the formation volume.

Embedded-atom method (EAM) type potentials approximate the material by a homogeneous gas of free electrons and a constant density derived from the nuclei. The atoms are thus embedded in

this model material, called jellium. EAM is a semi-empirical method, suitable for metallic systems with no directional bonding. Covalency, significant charge transfer and Fermi-surface effects are not considered. However, EAM potentials are an effective way to calculate the structural and energetic properties of metals [108].

Two EAM potentials for Fe-C are used in Paper **I**: one by C. S. Becquart and J. M. Raulot *et al.* (henceforth the Raulot potential) [109] and one by D.J. Hepburn and G. J. Ackland [110]. Both potentials use the Fe-Fe part by G. J. Ackland *et al.* [111], which is also of EAM type and known to be one of the best potentials for describing pure Fe and its lattice defects. The Raulot potential is a many-body potential fitted to *ab initio* data for Fe-C and C-C interactions in low concentrations of C in Fe. The potential was especially designed to reproduce the energy and forces acting on C atoms in tetrahedral and octahedral positions (*Cf.* 4.2). The Hepburn potential, also a many-body potential addressing Fe-C and C-C interactions, was developed to give correctly the interactions between C and SIA defects and the correct energetics of carbon-vacancy complexes, such as C_2V and CV_2; it correctly describes the angular dependent carbon-carbon interaction in bulk Fe and correctly reproduces a strong repulsion of carbon in the vicinity of a $\langle 110 \rangle$ dumbbell and the correct solvation energy of C in Fe, as obtained by *ab initio* calculations.

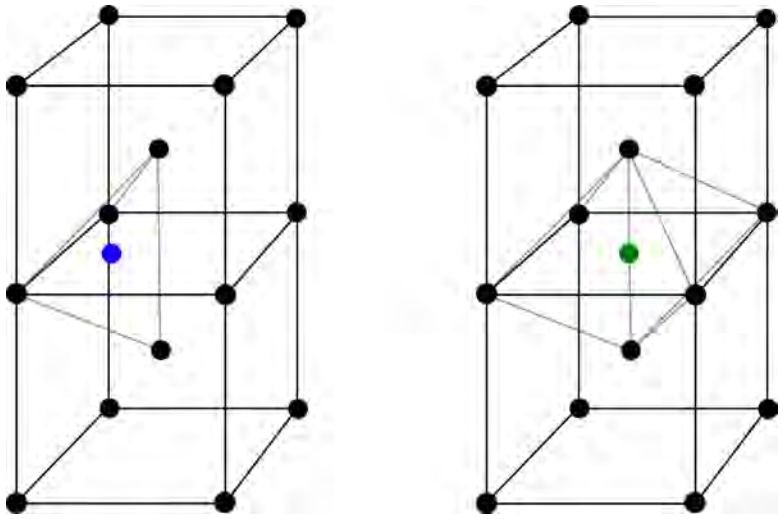

Figure 4.2: The tetrahedral (blue) and octahedral (green) positions in the bcc lattice.

The Johnson potential has been used in a large number of studies of the interaction of $1/2\langle 111 \rangle \{110\}$ edge dislocations, SIA clusters and vacancies with carbon [112–114]; making it a good reference potential, even though it does not take into account C-C interactions. The potential also significantly underestimates the solvation energy of C in Fe, i.e. the difference in the crystal energy with and without a C atom, giving 1.32 eV. The Raulot potential gives the overestimated value 10.05 eV, whereas the Hepburn potential correctly reproduces the *ab initio* value, 6.27 eV [110, 115]. The Raulot potential

reasonably reproduces the C-C interaction in comparison with *ab initio* data, but predicts a strong positive C-$\langle 110 \rangle$ dumbbell binding energy, whereas it should be negative according to *ab initio* calculations. The same problem occurs with the Johnson potential.

4.2 Object Kinetic Monte Carlo

The Monte Carlo Method was introduced by Stanislaw Ulam, John von Neuman and Nicholas Metropolis at the end of World War II at Los Alamos National Laboratory in New Mexico, USA, to study the diffusion of neutrons in fissionable materials [102, 116]. The name "Monte Carlo", coined by Metropolis, came from the extensive use of random numbers in the method, associating it with the famous casinos in Monaco.

The general idea of the Monte Carlo method is to formulate a problem in terms of probability distribution and then sample the distributions randomly, using a random number generator, to get an approximate result that will converge towards the exact answer with enough samplings. The principle is best illustrated by a simple example: The value of π can be approximated by randomly choosing points in a square with side length 1.0, as shown in Fig. 4.3. The blue area in the figure is the set of points that are under the curve $y = \sqrt{1-x^2}$, that is a 1/4 of a circle with the radius $r = 1.0$. If the random points are chosen uniformly between 0 and 1 for both the x and y dimension, the probability for choosing a point inside the blue area, inside the circle, is given by

$$\frac{\text{Blue area}}{\text{Total area (blue + green)}} = \frac{\frac{1}{4}\pi r^2}{1} = \frac{\pi}{4} \tag{4.8}$$

By counting the number of random points chosen in the blue area, N_b, and in the green area, N_g, we will see that the value of the fraction of the total points chosen in the blue area will converge towards $\pi/4$ with the growing number of random points. In the end we get that:

$$\pi \approx \frac{4N_b}{N_b + N_g}. \tag{4.9}$$

An important variant of the Monte Carlo method is the Metropolis Monte Carlo (MMC), described by N. Metropolis *et. al.* 1953 [117]. The random positions in the Monte Carlo example above were chosen randomly, completely independently of which points had been chosen before. We can formulate it more generally by saying that every new chosen random point in the system constitutes a new *state*, N_i, where i is the number of random points chosen in the system, i.e. the set of points inside the

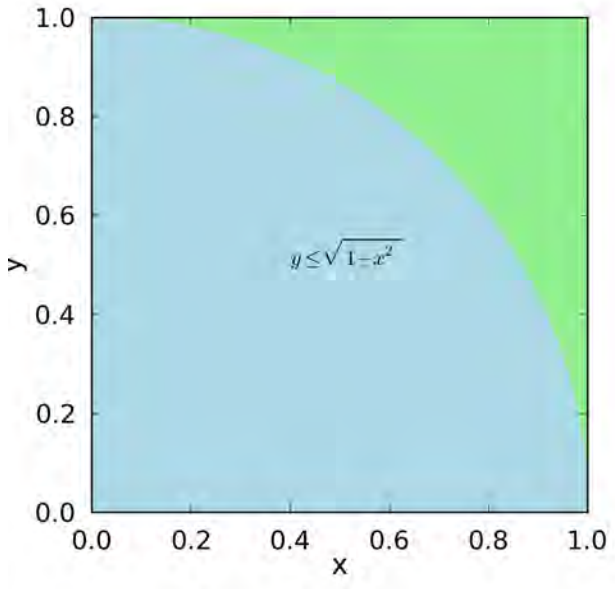

Figure 4.3: Geometric illustration of the probabilities for calculating π using Monte Carlo. All points in the blue area are below the curve $y = \sqrt{1-x^2}$ and thus have the area of 1/4 of a circle with a radius 1.

square area. A new state is not dependent on the former states, as a new point is chosen randomly. In MMC, however, new states depend on the previous states. MMC tries to maximize or minimize a function, $f(\mathbf{x})$, that depends on the state of the system, $\mathbf{x}$. As an example, the state of a system could be the coordinates of N atoms, $\{\mathbf{x_i}\}$ ($i = [1,N]$), in a gas or solid and the function could be the energy of the system, $E(\{\mathbf{x}_i\})$. The energy would depend on how close the atoms are to each other and the probability distribution of the system would be $\rho(E) = \exp(-E/(kT))$. To find the most energetically favourable configuration, we want to minimize E by starting from a random configuration $\{\mathbf{x}_i\}_0$ and vary the position of every atom randomly within a certain limit. After this, the new energy, E' is calculated for the system again and if the energy has decreased, $E' < E$, the new state (i.e. the set of positions $\{\mathbf{x_i}\}$) is accepted; if not, the new state is only accepted with a probability $\rho(E')/\rho(E)$. This is done by choosing a random number u between 0 and 1 and if $u < \rho(E')/\rho(E)$, the state is accepted and otherwise the system is reversed to the previous state. This cycle is repeated until equilibrium with the minimum energy E is reached and thus the most energetically favourable configuration $\{\mathbf{x_i}\}$ is found.

Kinetic Monte Carlo (KMC) builds further on top of MMC by taking time into account, which is what the word ”kinetic“ indicates here. In MMC, time is not considered at all. KMC can consider systems of atoms, called Atomistic KMC (AKMC); general objects or atomic clusters (as in this thesis), Object KMC (OKMC); or only events, Event KMC (EKMC). The key is that the probabilities for all possible events for all atoms or objects in the system are pre-defined in terms of frequencies

of events. The system will evolve according to these frequencies. OKMC is the main method in this work, but AKMC results from the literature have also been used.

In AKMC, a (generally rigid) lattice of atoms with possible defects like vacancies and SIA (two atoms at one lattice site) are simulated. The atoms or vacancies may jump to a neighbour site with a certain pre-calculated frequency, related to the energy barrier between the two sites. Since all possible energy barriers of every atom in the system need to be pre-calculated, this is one of the main restrictions on the system size that can feasibly be simulated. OKMC, on the other hand, does not consider every atom in the system, but rather concentrates on the defects and defect clusters themselves. Vacancy and SIA clusters are described in OKMC as objects of simplified shapes, such as spheres of toroids, with pre-calculated probabilities for diffusion and emission, related to the cluster sizes. Bulk atoms are not taken into account explicitly as in AKMC or MD, but a lattice may be used for possible object positions, which is indeed the case for the OKMC code, LAKIMOCA [92], used in this thesis. Other OKMC codes, such as BIGMAC [118], do not use any underlying lattice.

The basic algorithm for KMC [119–121], and in particular OKMC, is shown in Fig. 4.4. The system is initialized at time $t = 0$ with a random population of objects according to the desired densities. If cascades are used, the initial system might even be empty with the random population introduced with a cascade in the first simulation step.

The dynamics of the OKMC simulations are defined by the events. Events can be divided into internal and external events. An overview of all objects and events are shown in Fig. 4.5. Internal events are thermally activated events with a probability given by Arrhenius frequencies,

$$\Gamma_i^{int} = \nu_i \exp\left(\frac{-A_i}{k_B T}\right), \tag{4.10}$$

where A_i is the activation energy for event i, ν_i, the attempt frequency, T the temperature, and k_B, Boltzmann's constant. In this thesis, the possible internal events are the migration jump of a defect (e.g. a vacancy or SIA cluster), dissociation of a vacancy from a vacancy cluster, or dissociation from a generic trap. For migration, the activation energy equals the migration energy of the defect $A_i = M^\delta$, where, in the notation of this work, δ is v for vacancy clusters, i for SIA clusters, and f for foreign interstitial atom (FIA) clusters, i.e. carbon or carbon-vacancy clusters in this work. A list of all OKMC parameters and their notations are shown in Table 4.1. If the event is dissociation, the activation energy is the migration energy of the defect plus the binding energy of the defect to the parent cluster, $A_i = M^\delta + B_d^\delta$. Dissociation of a SIA from a SIA cluster is allowed, even though such an event is very rare. Only defects of size one may be dissociated in LAKIMOCA.

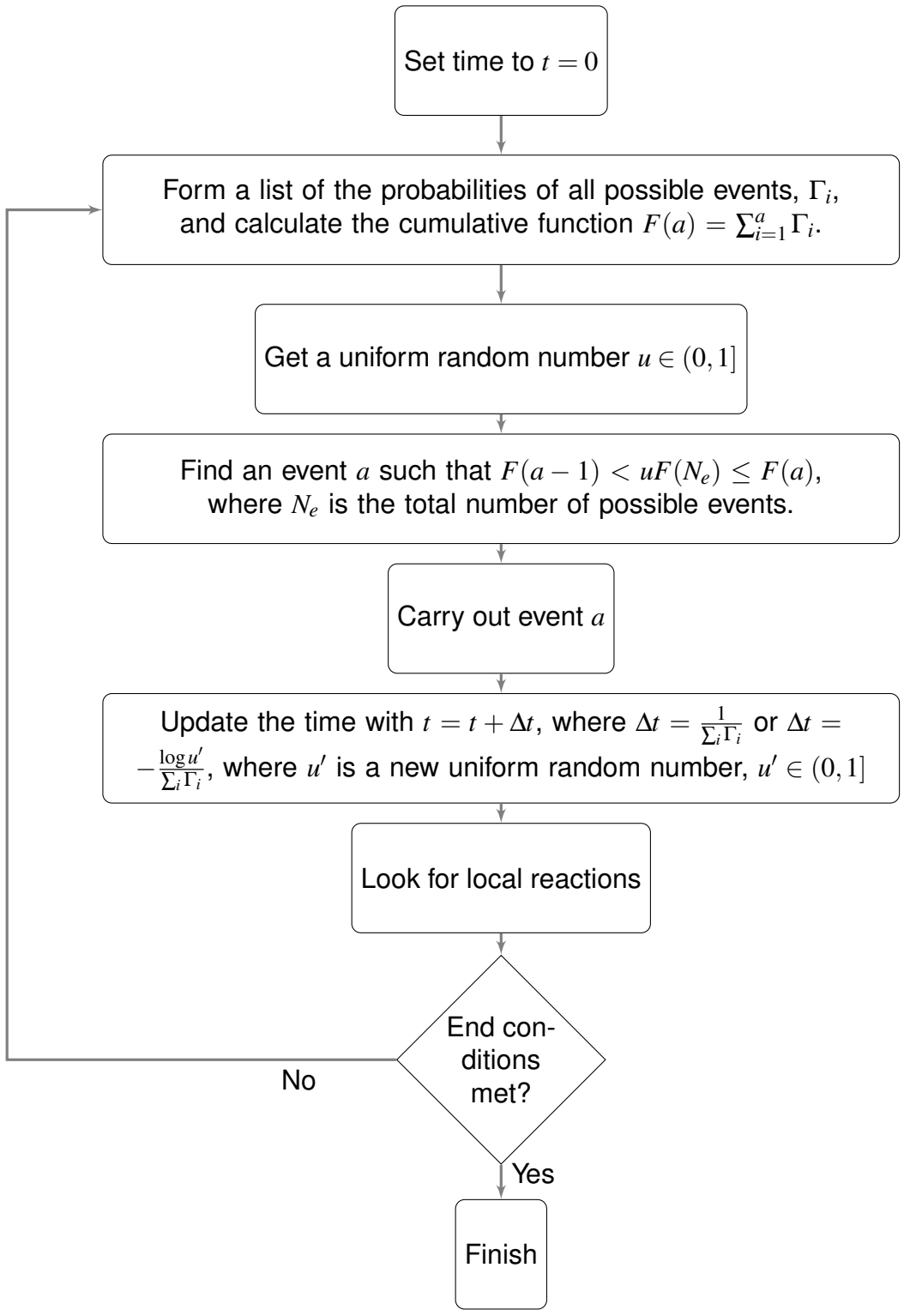

Figure 4.4: The basic residence-time algorithm used in OKMC.

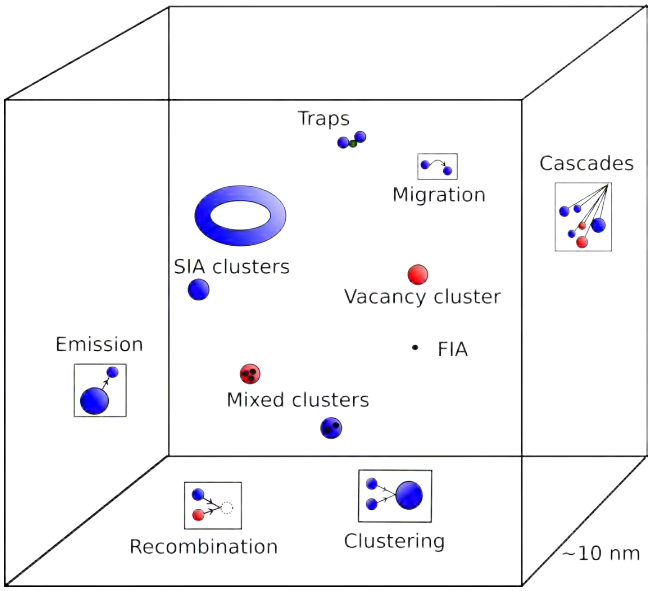

Figure 4.5: The OKMC simulation box with all objects and events used in the model. From Paper **III**.

Traps are immobile objects with an associated binding energy to either SIA or vacancy objects, $A_i = M_d^\delta + B_d^\delta$. The binding energy may depend on the cluster size. Dissociation of a cluster from a trap always means that the whole cluster is released. Dissociation of defects from trapped clusters is still possible if the parameters allow it. Since one type of trap can only trap one type of clusters, such as vacancy clusters, several different traps must be used in the same simulation. In this work, traps are used to simulate C and C-V clusters.

External events are not thermally activated, but are still introduced with a pre-defined probability (frequency), Γ_i^{ext}, in the simulations. Possible external events in this work are electron, neutron and ion irradiation. Electron irradiation is simulated by introducing Frenkel pairs (a vacancy plus an SIA) randomly into the system with a certain dose rate. It is assumed that one electron produces one Frenkel pair. Neutron and ion cascades are likewise introduced according to a specified dose rate. Cascade debris, consisting of SIA and vacancy clusters, are chosen randomly from a database of MD simulations of displacement cascades [53, 122–126]. The MD simulations were done using the Finnis-Sinclair potential for iron [127] and the used cascade energies ranged from 5 to 100 keV. The accumulated dpa is calculated using the NRT formula [92, 128]:

$$dpa = \frac{0.8E_D}{2E_{DT}}, \tag{4.11}$$

where E_D is the damage energy, the fraction of the kinetic energy of the primary knock-on atom (PKA) spectrum that is not absorbed by electronic excitation. This energy is well approximated by the cascade energy in the MD simulations. $E_{DT} = 40$ eV is the displacement threshold energy for Fe.

Table 4.1: Overview of the most important parameters for OKMC simulations and their annotations: $\delta = v$ for vacancy clusters, $\delta = i$ for SIA clusters, $\delta = f$ for FIA clusters, $\delta = fv$ for mixed FIA-vacancy clusters and $\delta = fi$ for mixed FIA-SIA clusters.

N^δ	-	The number of defects in the cluster — all parameters that follows are in principle functions of N^δ.
ν^δ	[s^{-1}]	The prefactor (or attempt frequency) for the cluster migration.
M^δ	[eV]	The migration energy of the cluster.
ν_d^δ	[s^{-1}]	The prefactor (or attempt frequency) for a emission of a defect, $d = i, v$ or f, from a cluster.
M_d^δ	[eV]	The migration energy of a defect, d, emitted from a cluster.
B_d^δ	[eV]	The binding energy of a defect d to a cluster
r^δ	[Å]	The capture radius around a given spherical object, representing its strain field; when two spheres overlap the two objects react with each other
χ^δ	-	Parameter determining the shape of the object. If 1, the geometrical shape of the cluster is a torus, if 0, the shape is a sphere.
η^δ	[eV]	The energy of rotation, used to define a pure probability (not frequency) of rotation of the Burgers vector associated with the cluster. A vanishing value corresponds to fully 3D motion, a value approaching 1 eV or more corresponds to fully 1D motion.
E_t^δ	[eV]	The energy by which a defect δ is bound by a generic trap.

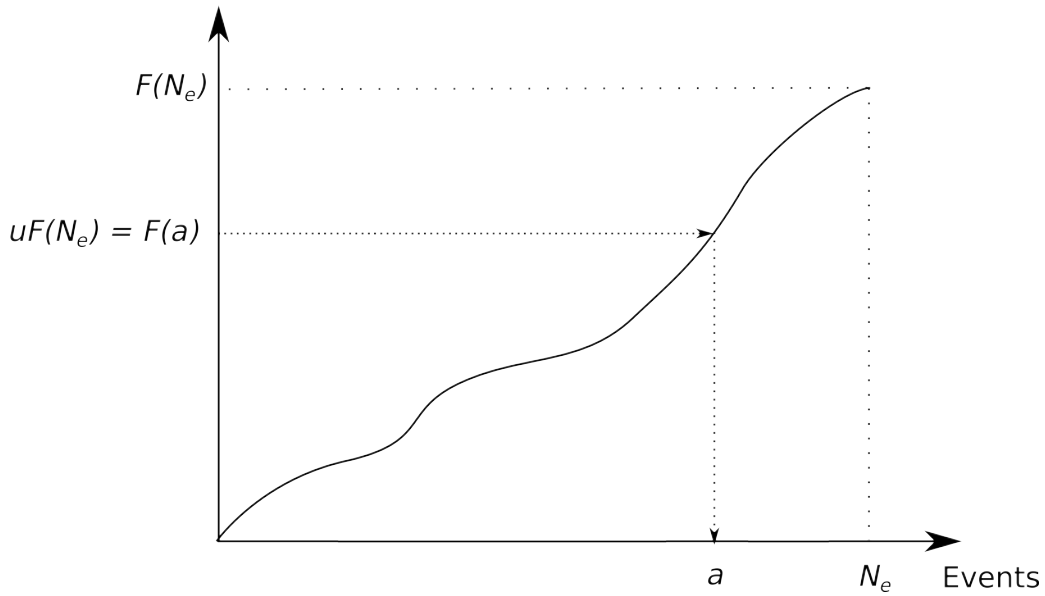

Figure 4.6: Schematic representation of the cumulative function of the probabilities of all events $i = 1 \ldots N_e$ in the system. Event a is chosen with a probability proportional to the probability of the event, $\Gamma_a = F(a) - F(a-1)$, using a random number $u = (0,1]$.

As seen in the second step in Fig. 4.4, the probability frequencies, $\Gamma_i = \{\Gamma_i^{int}, \Gamma_i^{ext}\}$ (in $[1/s]$), for all the possible internal and external events, $i = [1, N_e]$, at the current stage of the system need to be listed. A cumulative function of all possible events is calculated:

$$F(a) = \sum_{i=1}^{a} \Gamma_i. \tag{4.12}$$

An event a is chosen if $F(a-1) < uF(N_e) \leq F(a)$, where $u \in (0,1]$ is a uniform random number, as shown in Fig. 4.6.

After event a is carried out, the time change, Δt, has to be determined. This is done using the residence time algorithm [121],

$$\Delta t = \frac{1}{\sum_i \Gamma_i}, \tag{4.13}$$

where Γ_i are the probabilities for the possible internal and external events at this step. In the long time scale, it has been shown that Eq. (4.13) is equivalent to [120]

$$\Delta t = \frac{-\log u'}{\sum_i \Gamma_i}, \tag{4.14}$$

where $u' \in (0,1]$ is a uniform random number that takes more exactly into account the stochasticity of each event, assumed to follow a Poisson distribution. The OKMC simulations are thus not linear in

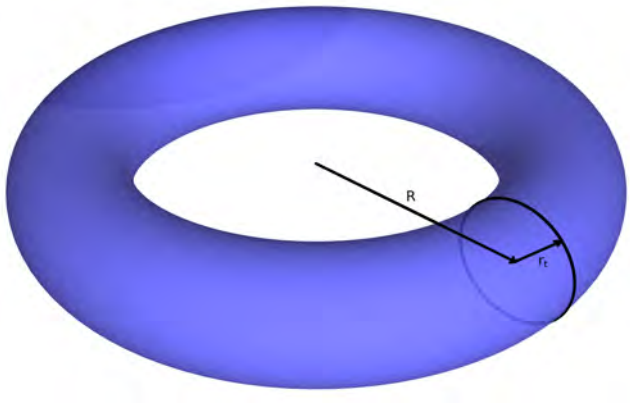

Figure 4.7: Depiction of a toroid with the major radius R and the minor radius r_t. From Paper **II**.

time, which can rather be seen as a decoupled parameter that will increase according to the average evolution of the system. It also means that the time scale may be short or long, depending on whether any fast-moving objects are present or only slow-moving objects are in the system. This feature enables OKMC to simulate processes that last from femtoseconds (fs) to years. After the time is updated as $t = t + \Delta t$, the system is checked for any reactions, that is, whether any two objects are near enough to each other to interact. As a last step, the end conditions are checked and, if they are not met, the list of probabilities will again be calculated and the cycle starts over again.

Reactions are not associated with a probability, but happen instantly if two objects overlap with each other, that is, if the capture radii, r^{δ}, of the respective objects overlap. Possible reactions are:

- Clustering of defects of the same kind (V or SIA).
- Annihilation, when one V cluster meets a SIA cluster. The new object will be the difference in size of the two parent clusters.
- Trapping, when a vacancy interacts with a vacancy trap or SIA with a SIA trap.
- Absorption at internal sinks or grain boundaries.

The object shapes, that play an important role for the reactions, are chosen to approximate the strain fields of the clusters. Vacancy clusters and small SIA clusters, FIA and mixed FIA-V clusters are approximated as spheres with capture radii, r^{δ}, that depend on the cluster sizes. Traps and sinks are also spherical with a fixed 5 Å radius. SIA clusters with more than 150 SIA, also called loops, are represented as toroids, shown in Fig. 4.7, with a major radius, R, that depends on the size of the cluster (*Cf.* Sec. 5.1.2) and a fixed minor radius, $r_t = 7.215$ Å, that corresponds to the capture radius of a 2-SIA (See Paper **III**).

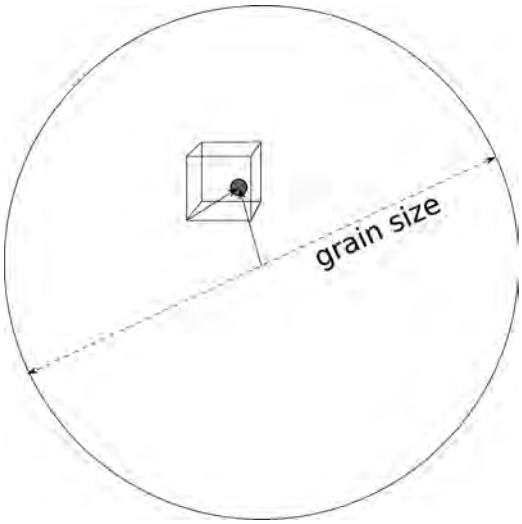

Figure 4.8: Treatment of the grain boundary in LAKIMOCA with one coordinate system for the simulation box and one for the spherical grain.

Grain boundaries separate the different crystals of homogeneous lattices in a metal and are sinks for both vacancy and SIA clusters, but not carbon. Typically, grains have a diameter that can vary from one to several tens or hundreds of micrometres (μm). In our OKMC code, LAKIMOCA, the grain is approximated by a sphere with a diameter of the average grain size [92, 129]. Defects are randomly distributed inside the sphere when introduced in the simulation by cascades or emissions, and removed when they migrate further than the grain boundary. Since the grain size is normally much larger than the simulation box, every defect will have two positions: one in the simulation box, to which periodic boundary conditions are applied, and one position in the grain, as shown in Fig. 4.8.

The simulation box in OKMC is normally a rectangular cuboid with sides typically 10 to 100 nm long. Cubic boxes should be avoided if 1D migrating defects are used, as this might lead to artefacts [129]. Periodic boundary conditions are normally applied in all three directions, making defects that reach the box boundary re-appear on the opposite side of the box.

OKMC only deals with rates and the simulated system is not required to be in thermodynamic equilibrium. The time scale is dynamic and the time step will vary depending on the objects present throughout the simulation; allowing simulations of time-scales as wide-ranging as fs to years with affordable computation time. OKMC scales computationally as $O(N^2)$, even though the number of objects, N, can vary considerably during one simulation. The main disadvantage of OKMC is that all probabilities for the included objects and events need to be known.

Chapter 5

Defect behaviour

In order to correctly build a model for the nanostructure evolution of irradiation defects in Fe-C, all defects need to be correctly characterized in order to know their stability, mobility and how they interact with each other. In Fe-C, the possible defects are vacancy and SIA clusters, carbon interstitial atoms and carbon-vacancy clusters, as already discussed in Sec. 3.3. The mobility of dislocations under load is dependent on the densities of irradiation-induced SIA and vacancy cluster populations, with high densities leading to reduced mobility and subsequent hardening and embrittlement of the material (see e.g. [13]). This thesis only deals with the evolution of the point defects and only considers the dislocations implicitly as sinks for vacancy and SIA clusters. The dynamics of dislocations is dealt with in higher order simulations, such as Dislocation Dynamics and Finite Element simulations, which can use the results of this thesis as input. This chapter summarizes how the vacancy, vacancy-carbon and SIA clusters are characterized and parameterized in order to construct an OKMC model for the defect evolution in Fe-C systems.

5.1 Characterisation of point defects in Fe-C systems

The important parameters needed for an OKMC model are listed in Table 4.1 and also already to some extent discussed in Sec. 4.2. Vacancy, vacancy-carbon and SIA clusters have a mobility characterized by an attempt frequency, ν^{δ}, and a migration energy M^{δ}, where in the notation of this thesis, $\delta = v$ for vacancy clusters, i for SIA, f for carbon and fv for vacancy-carbon clusters. The jump frequency of the clusters are given by the Arrhenius frequencies [130],

$$\Gamma(T) = \nu^{\delta} \exp\left(\frac{-A^{\delta}}{k_B T}\right), \tag{5.1}$$

where $A^\delta = M^\delta$ for migration jumps. The jump frequency is related to the diffusion coefficients by (see e.g. [130])

$$D(T) = D_0 \exp\left(\frac{-E_a^D}{k_B T}\right) = f_c(T)\frac{\Gamma(T) d_j^2}{2n}, \tag{5.2}$$

where D_0 is the diffusivity prefactor, E_a^D is the diffusion activation energy, f_c ($\sim$1 in the case of three-dimensionally randomly migrating vacancy clusters) is the correlation factor, d_j is the single jump distance, and n is the dimensionality of the migration (1 for 1D migration, 3 for 3D migration). Assuming $E_a^D = M^\delta$ and neglecting correlation effects, gives

$$D_0 \approx f_c \frac{\nu^\delta d_j^2}{2n} \approx \frac{\nu^\delta d_j^2}{2n}. \tag{5.3}$$

In the case of emission the jump frequency is also given by Eq. (5.1) with $A^\delta = E_{diss}^\delta = M_1^\delta + B_d^\delta$, where E_{diss}^δ is the dissociation energy and M_1^δ is the migration energy of a single emitted defect from the cluster. B_d^δ is the binding energy of the emitted single defect, d (= i, v or f), to the parent cluster, δ. Emission of a cluster is a very rare event and omitted in the model.

The stability of the clusters is characterized by the attempt frequency of emission of one defect d from the defect cluster, ν_d^δ, the migration energy of the defect, M_d^δ, and the binding energy of the emitted defect, B_d^δ. The volume of spherical cluster is determined by the capture radius, r^δ. Large SIA clusters are assumed to have a toroidal shape, indicated in the parameters by $\chi^i = 1$, which is 0 for spherical shapes. SIA clusters also have different migration regimes, ranging from fully 3D, $\eta^i = 0$, to fully 1D, $\eta^i \leq 1$. Finally, all clusters have a characteristic trapping energy, the binding energy to traps, E_t^δ, that can be different for different classes of traps. All these parameters are functions of the size in number of point defects in the clusters, N^δ.

5.1.1 Vacancy clusters

The parameterization of vacancy clusters is explained in detail in Paper **III**. The same parameters are used at both low and high temperature since there is no essential qualitative change in how vacancy clusters behave at different temperatures. This section summarizes how the parameters for vacancy clusters were chosen.

The migration energy for a single vacancy was chosen according to MD studies with the potential by M. Mendelev *et al.*: $M^v = 0.63$ eV [131]. As attempt frequency for migration and emission, the Debye frequency is used: $\nu^v = \nu_v^v = 6 \times 10^{12}$ s^{-1}. For vacancy clusters of larger sizes, results from AKMC

calculations from [132, 133] are used to get the attempt frequencies for migration and emission, the migration energy, and the binding energy. Since AKMC simulations are expensive and the needed values are only calculated for a selected number of clusters up to size $N^v = 250$, the values had to be interpolated using cubic splines and then extrapolated to get values for clusters of size $M^v > 250$. For the attempt frequency, the extrapolation was done by assuming the clusters to migrate by surface diffusion mechanisms, giving a size dependency of the form ([134], as in [135]):

$$\nu^v \sim \frac{\nu_1}{(N^v)^{4/3}}. \tag{5.4}$$

For the binding energy, B^v, the values were extrapolated using the function

$$B^v = 1.71\,\text{eV} + 3.39716[(N^v)^{2/3} - (N^v + 1)^{2/3}]\,\text{eV} \tag{5.5}$$

that has the formation energy of the vacancy, given by the Mendelev potential, as asymptote. The attempt frequencies and the migration energy parameters were extrapolated by linear functions.

All vacancy clusters of any size are in the model of this thesis described as spheres ($\chi^v = 0$) with the capture radius derived from Table 2 in [92]:

$$r^v = \frac{3.3a_0}{1+\gamma} + \varepsilon + a_0 \left(\frac{3}{8\pi}\right)^{1/3} \left((N^v)^{1/3} - 1\right) \tag{5.6}$$

with the interstitial bias $\gamma = 1.2$, $\varepsilon = 0.01$, and $a_0 = 2.87$ Å (the lattice parameter in iron). The main idea behind this formula is that the volume of the sphere should correspond to the volume of the number of vacancies it contains with the volume of a single vacancy given by its strain field. Experiments give that recombinations between a vacancy and a SIA occur at a distance of $3.3a_0$ (see refs. in [92]), which is taken into account in the equation. Also, the larger strain field of SIA clusters, compared to vacancy clusters, is taken into account with the bias factor γ. Recombination or clustering between two clusters occur in OKMC when two clusters, defined by their capture radii, overlap. The vacancy clusters always migrate in a fully 3D fashion and thus $\eta^v = 0$ for all sizes.

5.1.2 SIA clusters

SIA clusters are more complex to parameterize than vacancy clusters, as they can exist in different forms with different mobilities, shapes and stability. In Fe-C systems irradiated at low temperatures (<370 K), $1/2\langle 111\rangle$ SIA clusters are dominating, whereas irradiation at high temperatures (>500 K) results in (pre)dominance of $\langle 100\rangle$ SIA clusters, as already discussed in Sec. 3.3. The main difference

Table 5.1: The attempt frequencies, ν^i, and the migration energies, M^i, for SIA cluster sizes of N^i = 1–5. These values are used at all temperatures.

N^i	ν^i [10^{13} s^{-1}]	M^i [eV]	
1	8.071	0.31	(Exp. value)
2	34.15	0.42	(DFT and exp. value)
3	1.175	0.42	
4	1.195	0.8	
5	0.156	0.1	
6	0.156	0.05, 0.2	(low T, high T)
7	0.171	0.05, 0.2	(low T, high T)

between the two kinds of SIA clusters are in shape and mobility, which has to be taken into account, which is why two parameterizations for SIA clusters are used: one for low and one for high temperature. The parameterization for low temperatures is discussed in detail in Paper **III** and the modifications done for high temperatures are discussed in detail in Paper **V**. This section will summarize the two parameterizations.

The migration energy of a single SIA has been found experimentally and in *ab initio* calculations to be 0.3 eV in iron [136, 137] and migrate in a fully 3D fashion. SIA clusters of size 2–5 are more complicated as they might exist in a non-parallel configuration, as seen in MD simulations [138]. As the non-parallel configuration might be more stable, as in the case of the di-SIA, the effective migration energy would be the unfaulting energy, which is larger than the migration energy of the parallel configuration [90, 137, 138]. The processes of unfaulting SIA clusters of size 3–4 are not yet properly understood and hence the unfaulting energy is hard to calculate and still debated. MD calculations with the Mendelev potential provide reasonable estimates of $\sim$0.8 eV for 4-SIA, which is also used for the 3-SIA cluster in this model, as the existing estimate of $\sim$0.15 eV with the same potential seems to be an underestimation [138]. No values exist for size 5, which had to be extrapolated from the other values. The chosen migration energy values for SIA clusters of size 1–5 are shown in Table 5.1.

For SIA clusters above size 5, MD calculations give a value of $\sim$0.05 eV (see e.g. [48]) for $1/2\langle 111\rangle$ SIA clusters. Preliminary results estimate a migration energy of 0.9 eV for the $\langle 100\rangle$ SIA cluster [139]. However, since SIA clusters can not be observed if they are smaller than the TEM resolution, it can not be excluded that small invisible SIA clusters of both kinds exist at high temperatures. To simulate the existence of two kinds of SIA clusters at 560 K, an effective migration energy of 0.2 eV had to be calibrated (see Paper **V**) for SIA clusters of size $6 \leq N^i \leq N_{th}^{high}$, where $N_{th}^{high} = 90$ is the threshold parameter for the high temperature parameterization and also the chosen TEM resolution

size for visible SIA clusters. Above size $N_{th}^{high} = 90$, the migration energy value for $\langle 100 \rangle$ SIA clusters of 0.9 eV is used.

The attempt frequency for all SIA clusters of size 1–7 are derived using Eq. (5.3) and values from [90]. For sizes larger than $N^i = 7$, the formula

$$\nu^i = \frac{c}{(N^i)^{0.8}}, \tag{5.7}$$

was used. Here $c = 8.11 \times 10^{12}$ was fitted to give the same value for $N^i = 7$ as given in Table 5.1.

The emission of SIA is known to be a very rare event, but is not explicitly forbidden in the model. The migration energy of the emitted SIA is chosen to be the same as for a single SIA, 0.3 eV, and the attempt frequency for emission is the Debye frequency 6×10^{12} s^{-1}. The binding energy of the emitted SIA is given by the formula reported e.g. in [92]:

$$B_i^i(N^i) = e_{for} + \frac{(B_i^i(2) - e_{for})((N^i)^s - (N^i - 1)^s)}{2^s - 1}, \tag{5.8}$$

where $s = \frac{2}{3}$, $B_i^i(2) = 1.0$ eV is the binding energy of the di–interstitial, and $e_{for} = 4.0$ eV is the formation of the single interstitial.

SIA clusters smaller than $N^i = 150$ are approximated as a circular disk with a capture radius r^i. The capture radius of $1/2\langle 111 \rangle$ SIA clusters are calculated as

$$r^i = r_0^i + \frac{a_0}{\sqrt{\pi\sqrt{3}}}(\sqrt{N^i} - 1), \tag{5.9}$$

$$r_0^i = \gamma \frac{3.3 a_0}{1 + \gamma}, \tag{5.10}$$

where $\gamma = 1.2$. For the smaller $\langle 100 \rangle$ SIA clusters, the radius is given by

$$r^i = r_0^i + \frac{a_0}{\sqrt{2\pi}}(\sqrt{N^i} - 1). \tag{5.11}$$

For SIA clusters larger than $N^i = 150$, a toroidal shape ($\chi^i = 1$) is used with a minor radius (see Fig. 4.7) of $r_t = 7.215$ Å and a major radius given for the $1/2\langle 111 \rangle$ SIA clusters by

$$R = \sqrt{\frac{a_0^2 N^i}{\pi\sqrt{3}}} \tag{5.12}$$

and for the $\langle 100 \rangle$ SIA clusters by

$$R = \sqrt{\frac{a_0^2 N^i}{2\pi}}. \tag{5.13}$$

These equations are obtained by approximating the toroid by a circle with the same area as of N^i SIAs, which differs depending on the kind of SIA cluster.

Finally the dimensionality of the migration of the SIA clusters are taken into account with the η^i parameter that can be seen as a rotation energy, giving a probability of change of direction of a cluster according to the Boltzmann distribution, $\exp[\eta^i/(k_B T)]$. For clusters of size 1 and 2, $\eta^i = 0$, giving a fully 3D migration. For larger clusters, η^i is increased gradually until a fully 1D regime is achieved at size $\sim$12 with $\eta^i \geq 1$ eV (depending on the temperature).

5.1.3 Vacancy-carbon clusters

As already mentioned in Sec. 3.3, $1/2\langle 111 \rangle$ SIA clusters have been observed to be trapped by invisible obstacles with an estimated trapping energy of $\sim$1 eV. A part of this thesis project has been to try to identify these traps. An early candidate was carbon interstitial atoms, but it was shown in Paper **I** that one C atom is not enough to trap a $1/2\langle 111 \rangle$ SIA cluster: The binding energy between a single C atom and a SIA cluster is well below 1 eV and at least two C atoms would be needed to have a combined trapping energy of more than 1 eV. However, no drag of C atoms by SIA clusters was observed in the MD simulations and since an encounter of a SIA cluster with two C atoms simultaneously is very unlikely, as C atoms do not cluster, the possibility of strong trapping of $1/2\langle 111 \rangle$ SIA clusters by single carbon atoms was ruled out. It was also found in Paper **I** that the binding of a C atom differs significantly depending on which part of the SIA clusters it interacts with. The strongest binding was found to be with the edge of the SIA cluster, 0.47 eV for a 7-SIA cluster and 0.65 eV for a 61-SIA cluster, using the currently most reliable potential by Hepburn and Ackland [110] (henceforth the Hepburn potential). In the centre of both SIA clusters, no binding with the C atom was found.

Other candidates for the SIA traps were carbon-vacancy clusters. In order to determine the stability of such clusters, the binding energies between a C atom and a vacancy cluster of size 1–6 were calculated using potentials by Hepburn *et al.* [110], Becquart and Raulot *et al.* [109] and Johnson [104]. The binding energies between a vacancy and the same C-V complexes were also calculated (see Paper **I**). The binding energy between defect A and B is defined as $E_b(A,B) = E(A) + E(B) - E(A+B) - E_{perfect}$, where $E(A)$ is the total energy of the system (crystal) with defect A and $E_{perfect}$ is the energy of the system without any defects. The dissociation energy for C and V in small C-V clusters were

Table 5.2: Binding energies between C-V complexes and the edge or the centre of large SIA clusters (size 61 SIAs), according to MD simulations.

	$1/2\langle 111\rangle$ SIA binding energy [eV] [140]		$\langle 100\rangle$ SIA binding [eV] [141]
	Centre	Edge	
C	0.0	0.6 [Paper **I**]	1.1
CV	0.3	0.75	
CV_2	1.4	0.8	
C_2V	0.4	1.4–1.5	0.6

also calculated. The dissociation energy of defect A is defined as $E_{diss}(A) = E_b(A,B) + E_m(A)$, where $E_m(A)$ is the migration energy of defect A. It was found that according to the potentials by Johnson and Becquart *et al.*, C stabilises small vacancy clusters. However, the Hepburn potential predicts attractive interaction of a C atom only to clusters containing less than four vacancies.

OKMC simulations of the evolution of the trap candidate clusters during irradiation and annealing in Paper **III** revealed the CV_2 to be possibly the dominating cluster at low temperatures (<400 K) and the C_2V cluster to be dominating at higher temperatures. The regime change is due to the fact that the C atoms become mobile at ∼480 K and will cluster with the CV_2 complexes, which will then easily emit one vacancy each, leaving a population of C_2V complexes. MD calculations by Anento and Serra also showed later that the CV_2 complex have a strong binding of 1.4 eV with the centre of a $1/2\langle 111\rangle$ SIA cluster [140]. The SIA trapping energy, as calculated by Anento and Serra [140], of the small C-V clusters are shown in Table 5.2. At high temperatures (>450 K) only C_2V complexes are stable. The interaction of this complex with a $\langle 100\rangle$ SIA cluster has been studied with MD by Anento and Serra and they found a binding energy of only 0.6 eV [141]. The single C atom, however, binds with 1.1 eV to the $\langle 100\rangle$ SIA cluster [141], compared to only 0.6 eV with the $1/2\langle 111\rangle$ SIA cluster (see Paper **I**).

The conclusion is that different regimes of traps are needed: the trapping energy depends on the irradiation temperature, but does also change with temperature in case of annealing of a system irradiated at low temperature, as shown in Table 5.3. At low irradiation temperatures, below 450 K, only one kind of trap is used for SIA clusters, E^i_{t1}, but the trapping energy will depend on the size of the clusters. C-V complexes are more likely to interact with the edge of a sufficiently small SIA cluster, which at low irradiation temperatures are all of $1/2\langle 111\rangle$ type. The dominant traps are C, CV and CV_2 with binding energies of 0.6–0.8 eV to the SIA cluster edge. In the model SIA clusters with a size smaller than $N^{low}_{th} = 29$ are thus trapped with 0.6 eV. SIA clusters larger than N_{th} are more likely to be trapped by a CV_2 complex interacting with the centre of the cluster, which will be a much stronger trapping. For large SIA clusters, a strong trapping energy of 1.2 eV is thus used in the model. A higher value,

Table 5.3: Overview of the trap parameters for low and high irradiation temperature (below and above 450 K), as used in this model. All trapping energies are functions of the cluster sizes, N^{δ}. E^i_{t1} are SIA cluster traps used at both low and high irradiation temperatures, but with different thresholds: $N^{low}_{th} = 29$ at low irradiation temperature and $N^{high}_{th} = 90$ at high. In case of annealing of a system irradiated at low temperature, $E^i_t = 1.4$–1.5 eV for temperatures >450 K (see Paper **III**). E^i_{t2} are SIA cluster traps used only at high irradiation temperatures. E^v_t are vacancy cluster traps.

N^{δ}	E^i_{t1} [eV]	E^i_{t2} [eV]	E^v_t [eV]
1	0.17 [142]	0.6	0.65 [142]
2	0.28 [142]	0.6	1.01 [142]
3	0.36 [142]	0.6	0.93 [142]
4	0.34 [142]	0.6	0.96 [142]
5	0.60	1.2	1.23 [142]
6	0.60	1.2	1.20 [142]
7–N^{low}_{th}	0.6		0.4
N^{low}_{th} <	1.2–1.4, 1.4–1.5[a]		0.4
7–N^{high}_{th}	0.60	1.2	0.4
N^{high}_{th} <	1.1 [141]	0.6	0.4

[a] Only for system irradiated at low temperature, but annealed above 450 K.

like 1.4 eV found in MD simulations [140], could possibly be used, but the SIA clusters are already strongly trapped with 1.2 eV at low temperatures, so it would make no difference, as discussed in Sec. 6.1 and Paper **IV**.

If a system that has been previously irradiated at low temperature and thus contains only $1/2\langle 111\rangle$ SIA clusters is annealed to temperatures above 450 K, the trapping energy has to be adapted with raising temperature. Above 450 K, it was shown in Paper **III** that the C-V traps will change as C atoms become mobile at around this temperature. The dominating CV_2 will be transformed to C_2V complexes that trap SIA complexes with a binding energy of 1.4–1.5 eV. Annealing simulations in Paper **III**, which will also be more discussed in Sec. 6.1.3, show that a trapping energy of 1.4–1.5 eV is indeed needed for the large SIA clusters, which is both provided by CV_2 and C_2V, even though they bind with different strength to different part of the SIA clusters. It is worth pointing out that above ∼680 K, also the very stable C_2V complexes become unstable and only C atoms remain as weak traps.

At high irradiation temperature, two families of SIA traps are used, E^i_{t1} and E^i_{t2}, as also described in Paper **V**. The former trap family represents here the C atoms, that bind with 0.6 eV to the small $1/2\langle 111\rangle$ SIA clusters, which are assumed to be present, and with 1.1 eV to the visible $\langle 100\rangle$ SIA clusters, which are larger than size $N^{high}_{th} = 90$. The E^i_{t2} traps represent C_2V complexes that bind

strongly with 1.2 eV to the small SIA clusters, but weakly with only 0.6 eV to the large $\langle 100 \rangle$ SIA clusters. The value of 1.2 eV for small SIA clusters can be seen as an effective trapping energy, between 1.4 eV and 0.6 eV, as we assume both $1/2\langle 111 \rangle$ and $\langle 100 \rangle$ SIA clusters to be present.

Traps for vacancy clusters were also used at both low and high irradiation temperatures. At low temperature, only vacancy clusters smaller than $N^v = 7$ need to be trapped; a trapping energy of 0.4 eV was found to be necessary for larger vacancy clusters at high irradiation temperatures and could for consistency also be used at low irradiation temperatures, but it will have no impact on the nanostructure evolutions. The trapping energy for different vacancy cluster sizes are listed in Table 5.3.

5.2 Treatment of the dislocation density

Dislocations are not taken into account explicitly in the nanostructure evolution model. However, dislocations are sinks for small vacancy and SIA clusters and since the dislocation densities in the reference experiments considered in this thesis are very low, the effect of the dislocations has been approximated by spherical sinks instead of long cylinders that would be nearer to the real shape of dislocations. The sink strength for a particular dislocation density, ρ_d, may be expressed as [143]

$$k_d^2 = Z^\delta \rho_d, \tag{5.14}$$

where $Z^v = 1.0$ for vacancy clusters and Z^i is between 1.2 and 3.0 for SIA clusters, as discussed in Paper **V**. The sink strength of a spherical sink is given by [144]

$$k_s^2 = 4\pi R_s n_s, \tag{5.15}$$

where r_s is the spherical radius and n_s is the sink number density. The radius and sink density can now be chosen to give a sink strength equal to the sink strength of the dislocation density:

$$R_s^\delta = \frac{\rho Z^\delta}{4\pi n_s} - r_1^\delta, \tag{5.16}$$

where the capture radius of the single defect, r_1^δ, has been removed as the sink strength expressions are derived for dimensionless defects, which is not the case in OKMC simulations. We postulated that only clusters of sizes between 1 and 4 are affected by the dislocation sinks.

5.3 Sink Strength

An alternative to OKMC as a simulation method of the nanostructure evolution in materials is rate theory (RT), that uses differential equations for the rates of production and absorption of all defects in the system in a mean-field approach. By solving the complete system of differential rate equations, the evolution of the system can be calculated. The advantage compared to OKMC is that RT models use concentrations as variables, therefore the volume of the system is not a limiting factor. Moreover, precise equations are written, thereby being it possible to identify terms that can be neglected or to work out easily the steady-state regime. The disadvantage is that it is implicitly considered that events occur with the same rate everywhere in the volume (mean-field approximation), i.e. spatial inhomogeneities are not accounted for. Moreover, the intuitive and versatile objects in OKMC are replaced with abstract equations and rates, which requires more approximations to be introduced. For an overview of RT, see e.g. [29, 31].

RT and OKMC have been shown to be equivalent methods [145–147] and can in principle be used to solve the same kind of physical problems, as long as it is computationally feasible. The two methods can complement each other by giving different insight or dealing with different moments of the evolution of the system. Many analytical equations have been derived for RT, describing properties of irradiation defects, such as the absorption probability of a 3D migrating point defect by a sink, e.g. a dislocation loop. The rate of annihilation by a sink is in RT normally defined as Dck^2, where D is the 3D diffusion coefficient, c, the defect concentration and k^2 the sink strength. The sink strength is a very important parameter in RT, as it defines the rate at which a mobile defect interacts with a cluster or dislocation of a given shape and size. Many analytical expressions have been derived for the sink strength of absorbers of different shapes, such as spherical absorbers, toroidal absorbers and straight dislocations (see e.g. [144]).

In Paper **II**, we apply the OKMC method to test the analytical expressions for the sink strength of straight dislocations and dislocation loops for different sink densities, straight dislocation tubes of different size, and loops of different shapes and sizes. In OKMC the sink strength is calculated as [129]

$$k^2 = \frac{2n}{d_j^2 \langle n_j \rangle}, \tag{5.17}$$

where $\langle n_j \rangle$ is the average number of jumps performed by the defect, n is the dimensionality of the motion of the defect. In this work $n = 3$ is used consistently as we only compare with theoretical expressions derived using 3D diffusion coefficients. The jump distance d_j is defined in the bcc lattice

as the first nearest neighbour distance,

$$d_j = \frac{\sqrt{3}}{2} a_0. \tag{5.18}$$

The sink strength is calculated by introducing migrating defects one-by-one randomly in a simulation box with a population of identical sinks and count how many migration jumps are on average needed to reach a sink and be absorbed. Usually 10000–30000 defects are needed for good statistics.

The sink strength for an array of straight dislocation lines with 3D migrating defects is theoretically calculated to be [148]

$$k_{d,3}^2 = \frac{2\pi\rho_d(1-\rho^2)}{\ln\left(\frac{1}{\rho}\right) - \frac{3}{4} + \frac{1}{4}\rho^2(4-\rho^2)}, \tag{5.19}$$

where ρ_d is the dislocation density and $\rho = r_d\sqrt{\pi\rho_d}$. For toroidal sinks (such as SIA loops) with 3D migrating defects, the sink strength is given by [144]

$$k_{t,3}^2 = \frac{4\pi^2 n(R^2 - r_t^2)^{1/2}}{\ln(8R/r_t)}, \tag{5.20}$$

where R is the major radius and r_t the minor radius of the toroid (*Cf.* Fig. 4.7). In Paper **II**, we show that both these expressions are in excellent agreement with OKMC calculations, as long as, in the case of loops, r_t is small and R is between $2r_t$ and $15r_t$ and the sink volume fraction is low, as shown in Fig. 5.1. The sink volume fraction is the total volume of the sinks divided by the total volume of the system. For 1D migrating defects, the sink strength for dislocations is given by [38]

$$k_{d,1}^2 = 3 \cdot 2(\pi r_d \rho^*)^2, \tag{5.21}$$

where r_d is the capture radius of the dislocation cylinder and $\rho^* = \rho_d$ for a regular array of parallel dislocations. This expression was also verified with fair agreement using OKMC. No theoretical expression for 1D migrating defects and toroidal absorbers exist, but by adapting Eq. (5.21) for loops, we got an expression

$$k_{t,1}^2 = 6(n\pi^2 r_t R)^2, \tag{5.22}$$

that was in fair agreement with the OKMC calculations in the 1D case. However, the expression, Eq. (5.22), showed only fair agreement with 3D migrating defects.

Of particular interest, concerning the sink strength, is the transition from defects with a fully 3D migrating regime to defects with fully 1D migrating regime. The sink strength will change continuously

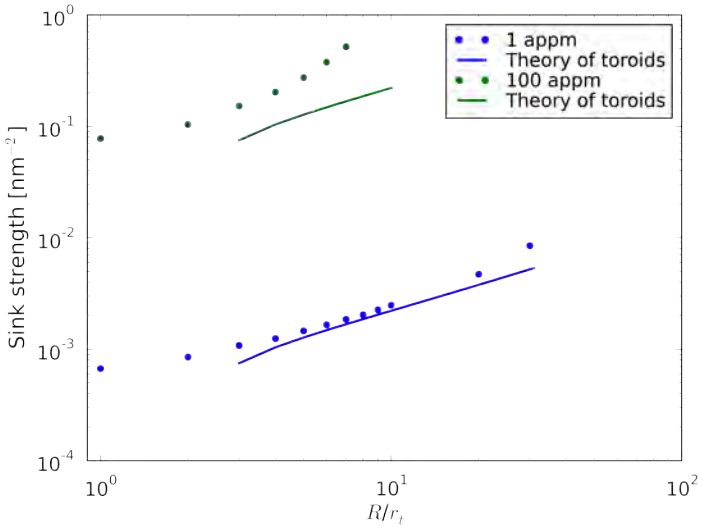

Figure 5.1: Sink strength of loops for two different number densities (distinguished by different colours), as a function of the ratio between the major toroidal radius, R, and the minor radius, r_t, which is here kept constant. The OKMC values are compared with the theory of loops, Eq. (5.20). From Paper **II**.

as the regime change from 3D to 1D, as has been shown for spherical absorbers [129]. The transition has been theoretically described using a master curve [149]:

$$y = \frac{1}{2}\left(1+\sqrt{1+4x^2}\right), \tag{5.23}$$

where x and y are defined as

$$x^2 = \frac{\frac{\delta f^2(\delta) l_{ch}^2 k_3^4}{12k_1^2}+1}{\frac{l_{ch}^2 k_1^4}{12k_1^2}+1}\left(\frac{k_3^2}{k_1^2}\right)\left(\frac{k_3^2}{k_1^2}-1\right), \tag{5.24}$$

$$y = \frac{k^2}{k_1^2}. \tag{5.25}$$

Here k_3^2 is the sink strength in the 3D limit, k_1^2 the sink strength in the 1D limit, k^2 the sink strength for a given $l_{ch} = d_j\sqrt{n_{ch}}$, the distance travelled in 1D before change of direction, with n_{ch} being the number of jumps before change of direction. The term $\delta f^2(\delta) \sim 0$ as transversal diffusion is not accounted for in our OKMC calculations. To calculate the sink strengths of the whole transition from fully 3D to 1D is computationally very heavy. The calculations took more than two months for the dislocation loops, but the results were in excellent agreement with Eq. (5.23), as shown in Fig. 5.2. For straight dislocations, only fair agreement was found, as the transition seems to be faster than the theory predicts.

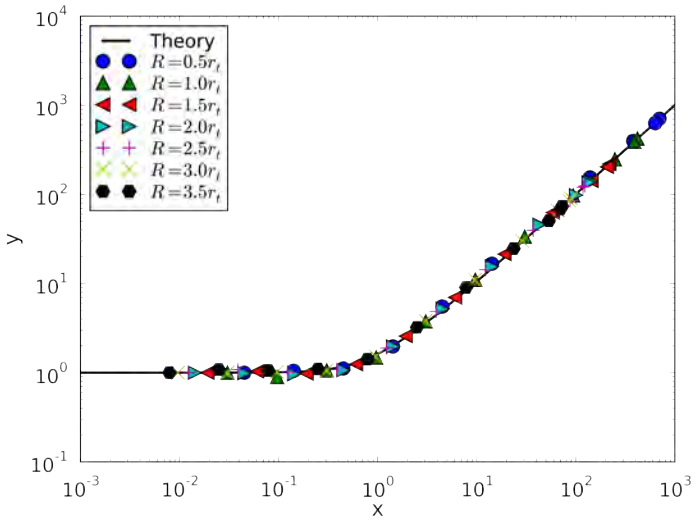

Figure 5.2: The master curve for different toroidal major radii, compared to the master curve, Eq. (5.23). From Paper **II**.

Paper **II** shows that OKMC results are in good agreement with theoretical results for dislocation loops and straight dislocations, derived for RT. In particular, since the master curve earlier has been shown to be satisfied with spherical absorbers [129] and now also for dislocations and dislocation loops, the master curve is now confirmed by OKMC to work for absorbers of any shape.

Chapter 6

Nanostructure evolution in irradiated Fe alloys

The previous chapter described how the defects present in iron under irradiation, such as vacancy and SIA clusters and carbon-vacancy clusters, have been characterized and parameterized. This chapter will consider how the populations of these clusters evolve over time, under irradiation conditions or during isochronal annealing, in terms of cluster densities and size distributions, i.e. the nanostructure evolution of Fe-C, using the modelling approach described in Sec. 4.2. The first Sec. 6.1 will describe how the model was developed for the low and high temperature systems and how the model was verified by comparing with experimental results. In Sec. 6.2, the model is applied by exploring the sensitivity of some of its parameters and some environmental parameters, such as the carbon content in the matrix and the irradiation dose rate.

6.1 Development of the model

The work flow for developing an OKMC model is schematically described in Fig. 6.1. The first part is to characterize all defects and defects clusters that will be introduced as objects in the model. For every object, the mobility and stability of the cluster it represents have to be known in order to determine the probability for all processes in the system, as described in Sec. 4.2. These defect properties are obtained by performing simulations with a higher accuracy than OKMC, such as MD, AKMC, RT or *ab intio* calculations; or by gathering available data from the literature. The most reliable data is collected into a set of parameters that will describe all objects and processes in the model and is thus the core of the OKMC model. The parameterization of the model of this thesis have already been discussed in Secs. 5.1 and 5.2 and is also described in detail in Paper **III** and **V**. The second part of the development process, which will be described more in detail in this section, is to verify the model

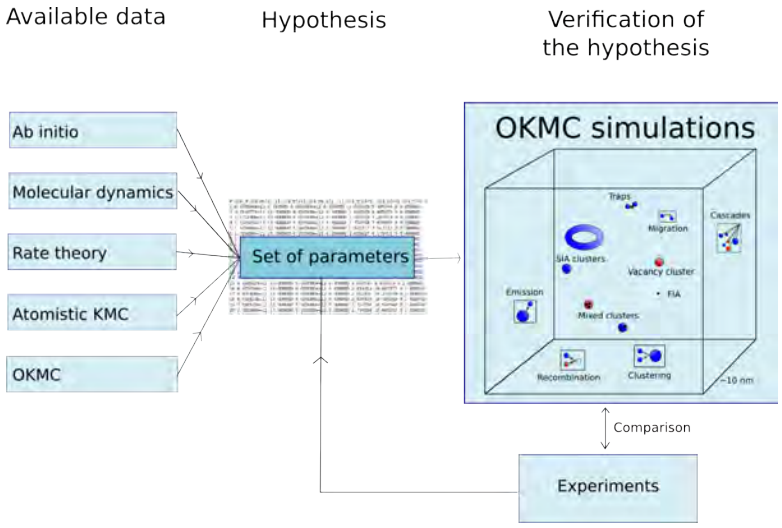

Figure 6.1: The work flow for developing a parameterized OKMC model.

by running the simulations using the parameterization and then compare with available experimental results.

The most exact way to simulate the nanostructure evolution in Fe-C would be to represent all defects as objects in the model, with all interactions described explicitly in the parameter set. This is, however, numerically cumbersome and in any case not all parameters are known for all objects. In this model, therefore, only vacancies and SIA clusters are represented by objects, while C and C-V complexes are described as immobile traps for vacancy and SIA clusters. In order to simulate C explicitly as an object, the binding energy with both vacancy and SIA clusters of all sizes needs to be known, which is far from the case today. Especially for the interactions between C-V clusters and SIA, only a few cases have been studied, as discussed in Sec. 5.1.3. However, Paper **III** presents results from simulations where C is indeed described explicitly, although in a simplified model, where the SIA clusters were excluded and only six different C-V complexes (including single V and C) were allowed. These simulations were done in order to estimate the evolution under irradiation, as well as for different temperatures (*Cf.* Fig. 6.2), of the small C-V clusters, that are believed to be traps for SIA clusters. This way, it could be seen that C and CV_2 complexes dominate at $<$450 K, whereas C and C_2V complexes dominate at higher temperatures up to $\sim$700 K, at which point even the C_2V complexes will dissociate to V and C. The final complex densities are depending on how many free C atoms are left after the irradiation stage.

As only C, CV_2 and C_2V play a major role as trapping complexes, representing these as static, immobile traps is a good approximation. As different C-V complexes dominate at different temperatures, different trap regimes at low and high temperatures are necessary. Another difference to take into account is that in iron irradiated at a temperature below 370 K, all SIA loops observed had $1/2\langle 111\rangle$

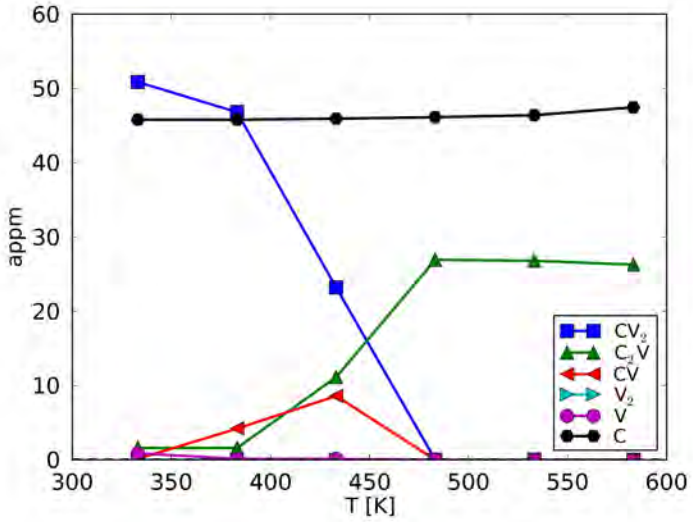

(a)

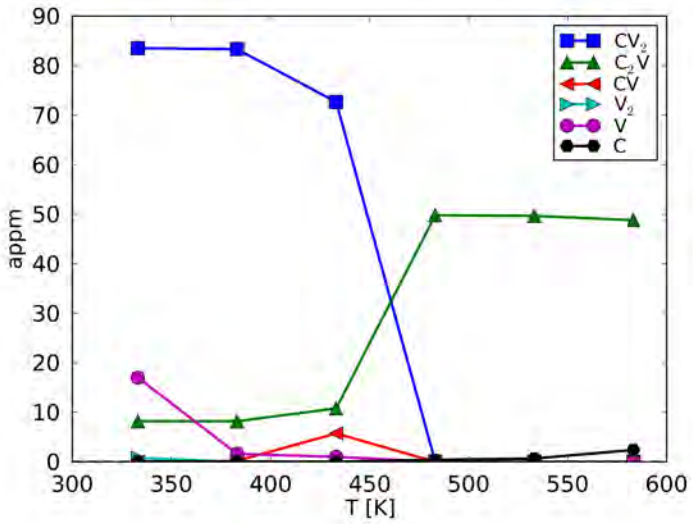

(b)

Figure 6.2: Annealing of a (a) carbon-dominated and (b) vacancy-dominated system of small C-V complexes to obtain the temperature dependence. From Paper **III**.

Burgers vectors, whereas when irradiated at 550–600 K, almost all loops had $\langle 100 \rangle$ Burgers vectors. These two families of SIA clusters have different mobility and different binding energy with C-V clusters, as discussed in Sec. 3.3 and 5.1.2.

6.1.1 Irradiation of Fe-C at temperatures below 370 K

For low temperatures, the model was verified in Paper **III** by reproducing the experimental results by Eldrup *et al.* [44, 76], who irradiated near-pure iron (about 80 appm C and N) at 343 K up to 0.23 dpa. This experiment was chosen as reference as it provides the most complete data for the vacancy and SIA density and mean size evolution versus dose at low temperatures, as they report both PAS and TEM results.

At this temperature all SIA clusters are assumed to be $1/2\langle 111 \rangle$, as was indeed observed in [44], and the traps are assumed to be C and CV_2. C binds to the edge with 0.6–0.7 eV and not at all to the centre of a $1/2\langle 111 \rangle$ SIA cluster (see Paper **I** and [140]) and CV_2 binds to the edge with 0.8 eV and with 1.4 eV to the centre. There are thus two cases with weak and strong trapping of the SIA clusters, depending on where the cluster binds with a C-V complex. Since small SIA clusters are much more likely to bind to the edge and large clusters are more likely to bind to the centre, we made the trapping energy depend on the size of the SIA clusters, so that SIA clusters below size N_{th}^{low} were trapped by a weak trapping energy, 0.6 eV. SIA clusters above size N_{th}^{low} were trapped with a strong trapping energy, chosen to be 1.2 eV, as the exact trapping energy of the CV_2 complex was not known at the time. We later saw in Paper **IV**, that at 343 K, a trapping energy above 1.2 eV (e.g. 1.4 eV, as calculated in [140] with the interatomic potential from [110]) does not change the results. The N_{th}^{low} threshold parameter is the only calibration parameter of the model and the best fit was obtained with $N_{th}^{low} = 29$, which agrees with the calculation in Paper **IV** that the probability for interaction with the edge SIA in the cluster is about 50 % with clusters at size 19–37. The N_{th}^{low} calibration parameter is thus physically motivated. Without the size dependence of the traps, all SIA clusters would coalesce into a single large cluster, independently of the simulation box size, which is not physical. This was also observed by Lee *et al.* [150], even though they used another mechanism for the size dependence than in this model.

The traps are not mobile in LAKIMOCA, which is not a problem as C atoms are not mobile at 343 K. The mobility of CV_2 is not known, but it is unlikely that the complex is mobile at this temperature. No trapping of vacancy clusters of sizes above 6 was used, but results at high temperature, 563 K, (see Paper **V**) suggested that a weak trapping energy of 0.4 eV of vacancy clusters larger than size 6 is needed. Using such a trapping energy also at 343 K does not change the results as the vacancy clusters at this low temperature are already rather immobile, as was reported in Paper **V**. The trapping

energy of vacancy clusters of size 1–6 are shown in Table 5.3. The vacancy traps are representing the same C-V complexes as the SIA traps, but in LAKIMOCA different traps have to be used for SIA and vacancy clusters. Since the OKMC simulations only deal with rates, using two separate populations of traps is not a problem as long as the defects are trapped with the right probability.

With these approximations, we showed in Paper **III** that the vacancy evolution is correctly reproduced in terms of number density and mean size (*Cf.* Fig. 6.3). The SIA density is also reproduced with good agreement with the reference experiment (*Cf.* Fig. 6.4), but the mean size for visible SIA clusters is generally overestimated by the model (*Cf.* Fig. 6.5). However, the reported experimental mean SIA sizes, obtained with TEM, are surprisingly small; the smallest mean size being only ∼1 nm and the reported TEM resolution 0.5 nm, whereas the normal TEM resolution is around 1.5 nm. It is thus possible that the mean SIA cluster size is underestimated in the experiments. Comparing the evolution with TEM results of the SIA cluster evolution is also generally problematic as the data are rather scarce, scattered and the density error bars are usually not reported, but can be assumed to be around half an order of magnitude.

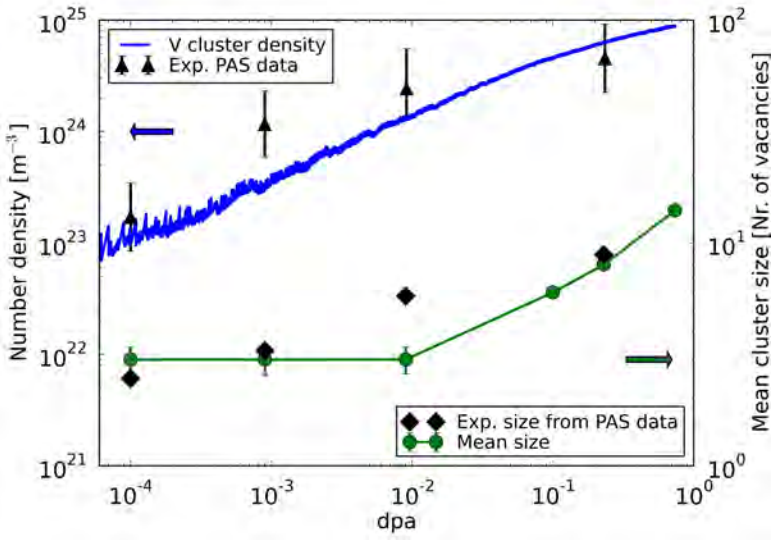

Figure 6.3: The vacancy cluster number density and mean size evolution versus dpa at 343 K. The experimental data are from [76]. From Paper **III**.

6.1.2 The nanostructure evolution under irradiation at 560 K

The model was verified for high irradiation temperatures in Paper **V** by comparing with experiments from the REVE campaign [39–41, 46, 83–86], where iron with about 134 appm C and N was irradiated

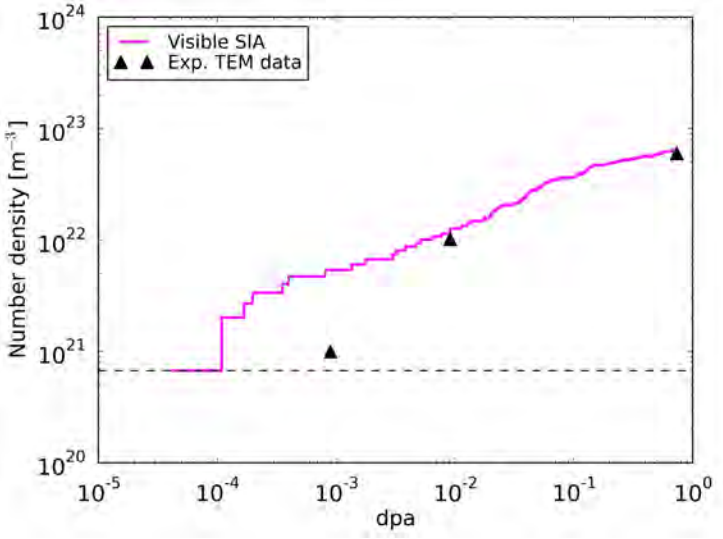

Figure 6.4: Number density of visible SIA versus dpa at 343 K. The experimental data are from [44]. The dotted line corresponds to one cluster in the simulated volume.

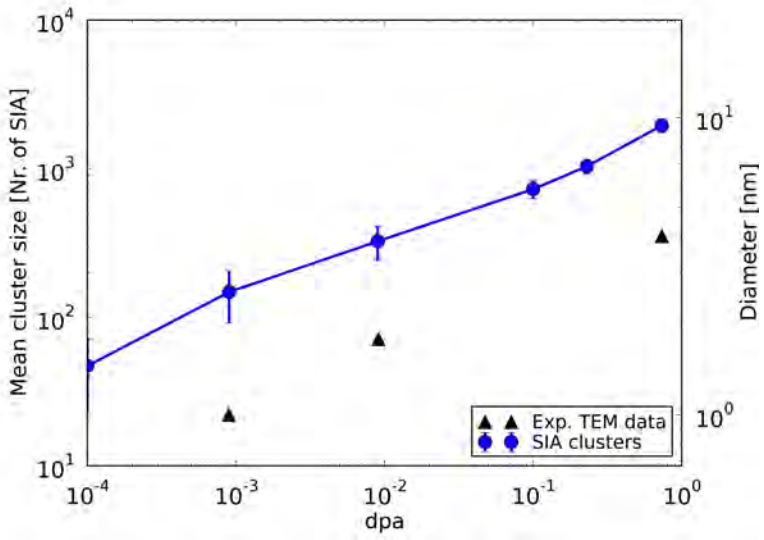

Figure 6.5: The SIA cluster mean sizes and their standard deviations for different dpa at 343 K. The experimental data are from [44]. From Paper **III**.

to 0.19 dpa at 563 K. For this experiment, the vacancy clusters are extensively studied with PAS, SANS and TEM, and the density and mean size evolution for SIA clusters is also studied with TEM.

At this high temperature, almost all experimentally observed SIA loops were of $\langle 100 \rangle$ type. However, since MD simulations have observed $1/2\langle 111 \rangle$ SIA loops to be created in cascades, it can be assumed that small SIA clusters of both kinds exist in the system, but only the $\langle 100 \rangle$ SIA clusters grow to become visible loops. The main assumption of the model at high temperature is thus that the SIA

loops below the visibility threshold size, N_{th}^{high} might be a mixture of the two kinds of SIA clusters, whereas the SIA clusters above size N_{th}^{high} are all of $\langle 100 \rangle$ type. Consequently, the migration energy of the visible SIA clusters is 0.9 eV [139] and for invisible sizes an effective migration energy of 0.2 eV was fitted. SIA clusters of size 1–6 are not assumed to have a Burgers vector and their migration energy is the same as in the lower temperature simulations, presented in Table 5.1. A more exact description of the system would, of course, have been to use two different families of SIA clusters. However, since it is not well known how $\langle 100 \rangle$ SIA clusters are created, and at which rate, and as the dynamics between the two kinds of SIA loops is not fully explored either, this kind of model would have to have other kinds of approximations instead and eventually many more uncertainties.

The traps are assumed to be C atoms and C_2V, as these are the only stable complexes at high temperatures, as discussed in Paper **III**. The trapping energy is different for the two kinds of SIA clusters and thus the trapping energy will be different for invisible and visible clusters. Two populations of traps were used, corresponding to C and C_2V. The used trapping energies are shown in Table 5.3. It can be seen that the E_{t1}^i trap is weak for invisible clusters, but strong for visible ones, whereas the E_{t2}^i is the other way around. As trapped clusters grow, they will be briefly released when they reach the N_{th}^{high} threshold size, only to be trapped again by another stronger trap. This mechanism promotes growth of large clusters. The threshold parameter was fitted to be $N_{th}^{high} = 90$, which corresponds quite well to the experimental TEM resolutions, 1–2 nm. The vacancy traps that correspond to the same C-V clusters as the SIA traps, were, however, only of one kind with the small clusters (size 1–6) trapped by the same energy as at low temperature and the larger clusters trapped with a small energy, fitted to be 0.4 eV. The energy of the vacancy traps are listed in Table 5.3.

The bias factor Z^i for the radius of the SIA sinks, as compared to vacancy sinks, given by Eq. (5.16), proved to have a significant effect on the SIA cluster evolution. This value is normally set to be 1.2–1.5, but it was found that a higher value of $Z^i = 3.0$ was needed. This could possibly be due to the fact that the mobility of C atoms is not explicitly taken into account in the model, as all traps are immobile. Several mobile C atoms could possibly bind to the same SIA cluster and thereby reduce the number of nucleation points in the material. As this is not possible in the model, it might be that the overestimated strength of the sinks, by the large bias Z^i, is compensating for this limitation of the model by decreasing the nucleation process. The main effect of the Z^i is to delay the visible SIA cluster growth, as discussed in Paper **V**.

Fe-C under irradiation at 563 K proved to be a more complex system to model than at 343 K, as the SIA and vacancy clusters at high temperature are much more dependent on each other than at low temperature. Changing e.g. the trapping energy of vacancy clusters, E_t^v, has a significant effect on the SIA cluster evolution. The model was constructed for high temperature by fine-tuning three calibration parameters: the migration energy for invisible SIA clusters, M_s^i; the visibility threshold,

N_{th}^{high} and the SIA sink bias, Z^i. Finding perfect agreement for both the density and the mean size evolutions with the experimental data proved difficult, so a compromise solution had to be found that was still physically defendable. Good agreement with both PAS and SANS data was found for vacancy densities (*Cf.* Fig. 6.6), as well as for SIA cluster density compared to TEM data (*Cf.* Fig. 6.7). The vacancy mean sizes are slightly overestimated (*Cf.* Fig. 6.8), compared to PAS and SANS, whereas the SIA mean sizes are slightly underestimated (*Cf.* Fig. 6.9). However, fair agreement with experiments is still reached for both the vacancy and SIA cluster mean sizes, as shown in Paper **V**.

6.1.3 Isochronal annealing of the pre-irradiated Fe-C system

The third way to test the model was to simulate the post-irradiation annealing experiment by Eyre and Bartlett [42], who used iron irradiated at 333 K and then annealed the material by slowly raising every hour the temperature until it reached ∼770 K. They report the visible SIA cluster density and the estimated density of SIAs in visible clusters (SVC). Since the irradiation was done at low temperature, only $1/2\langle 111\rangle$ SIA clusters were observed.

The annealing part of the simulation, as reported in Paper **III** and shown in Fig. 6.10, was divided into three stages to take into account the change of trap regimes from C and CV_2 complexes below 450 K, to strong C_2V complexes above, until they dissociate at around 680 K, leaving only C atoms. In the simulation, the temperature was raised every 1 h by 50 K. At the first stage, the small SIA clusters were trapped with 0.6 eV (except size 1–6, which always have the trapping energies listed for E_{t1}^i in Table 5.3) and SIA clusters larger than $N_{th}^{low} = 29$ were trapped with 1.2 eV, associated with the strong CV_2 complexes. MD simulations later gave a higher value of 1.4 eV for the trapping energy of the CV_2 with SIA clusters [140], which would not have changed the results of the simulations as 1.2 eV is already a very strong trapping energy at <483 K.

At the second stage, at the temperature range of 483–683 K, the best results were obtained by assuming a trapping energy of 1.4–1.5 eV to the second stage, which is in perfect agreement with the MD results for CV_2, bound to the centre, or a C_2V complex, bound to the edge of a SIA cluster [140]. At this stage, C atoms become mobile and the CV_2 complexes transform into the more stable C_2V complexes. The high trapping energy prevents the large SIA clusters, that had emerged during the first and second stage due to coalescence, from disappearing to the sinks. At the third and last stage, it was assumed that the only remaining traps were the weak C atoms, as the C_2V complexes, the most stable ones, would be the last to dissociate. At this stage the last SIA clusters disappear to the sinks and their densities drop considerably, in agreement with the experimental data.

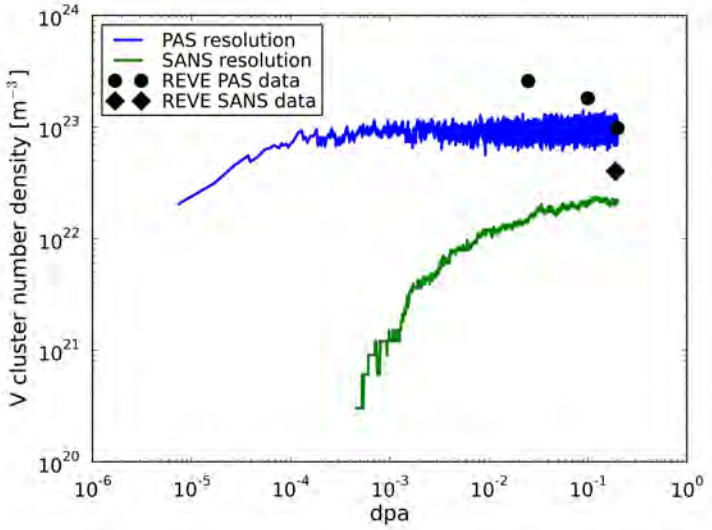

Figure 6.6: Density of vacancy clusters of sizes observable by PAS and SANS, respectively, versus dpa at 563 K. The data are compared with PAS [39, 41] and SANS data [86] from the REVE campaign. From Paper **V**.

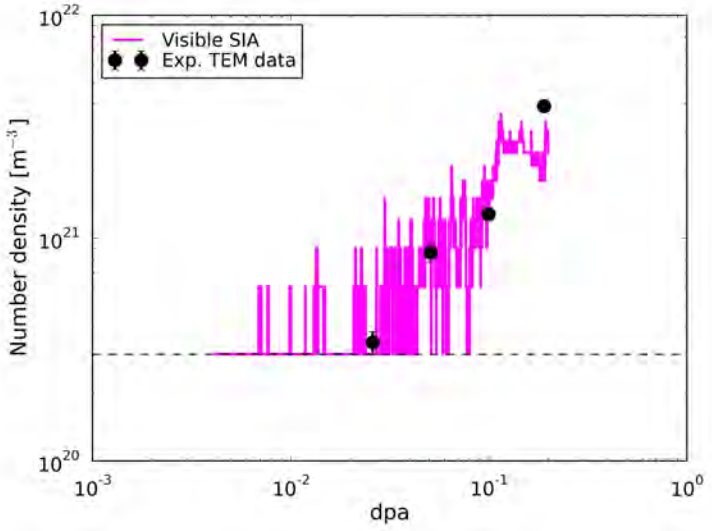

Figure 6.7: Visible SIA cluster density evolution versus dpa at 563 K. The experimental TEM data are from [46]. The dotted line corresponds to one cluster in the simulated volume. From Paper **V**.

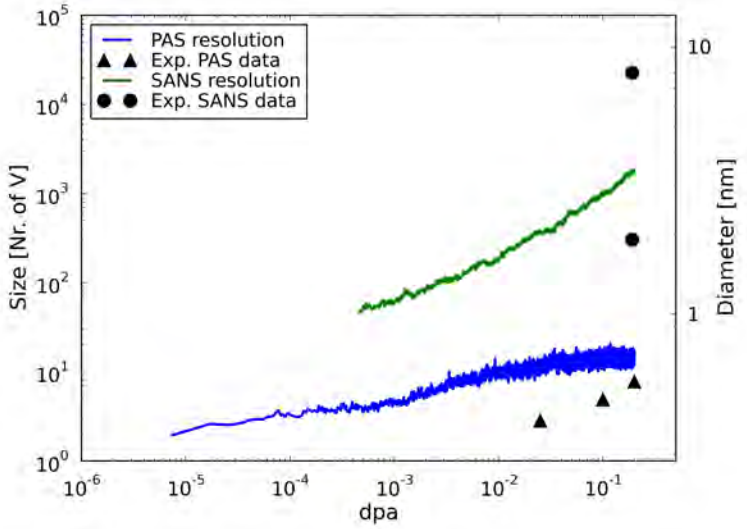

Figure 6.8: Vacancy cluster mean size versus dpa at 563 K with PAS and SANS resolution. The experimental PAS data (triangles) are from [39, 41]. The SANS data (bullets) show the two peaks of the size distribution at 0.2 dpa from [86]. The lower SANS data point is the major peak. From Paper **V**.

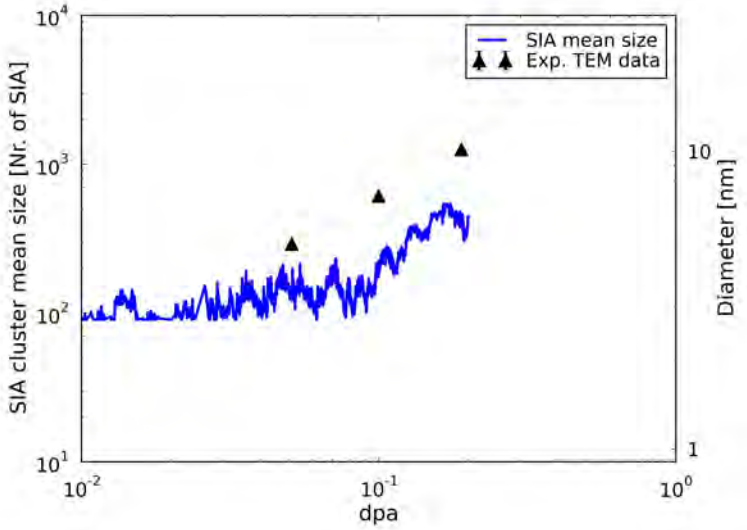

Figure 6.9: Visible SIA cluster mean cluster size evolution versus dpa at 563 K. The experimental TEM data are from [46]. From Paper **V**.

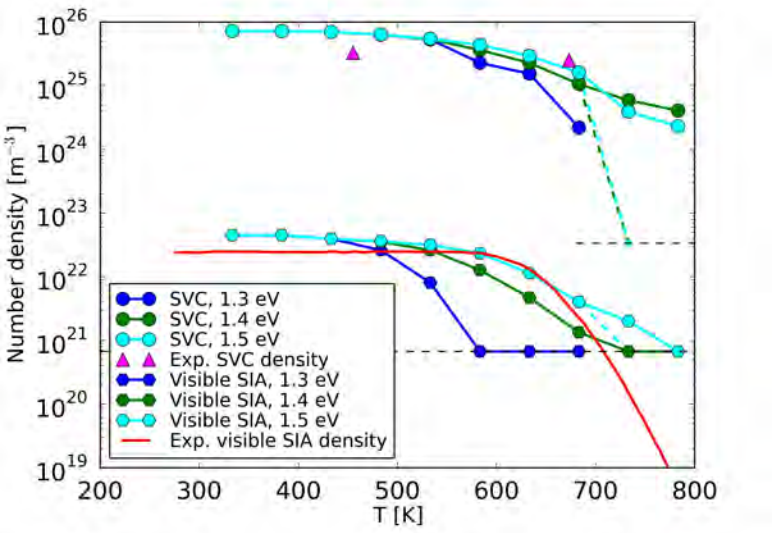

Figure 6.10: The density of visible SIA clusters and SIA in visible clusters (SVC) as a function of temperature during the simulated isochronal annealing. Different trapping energy for SIA, $E_t^i = 1.2$–1.5 eV, are used at the temperature of 483 K and higher. Above 733 K, if the trapping energy was decreased to $E_t^i = 0.6$ eV, all clusters disappear, as indicated by the dashed coloured lines. The solid line and the triangular dots are the experimental visible SIA cluster density and the SVC density, respectively, from [42]. The latter points are calculated from the reported visible SIA densities and the cluster diameter data. The dotted black lines indicate the density corresponding to one object in the box (lower line) and the minimum SVC simulation resolution (higher line), respectively. From Paper **III**.

The model managed to reproduce the visible SIA density and the SVC evolution with fair agreement to the experimental data.

6.2 Application of the model

In the first part of this chapter, it was shown that the model reproduces experimental data for both low and high irradiation temperature, as well as for post-irradiation annealing. It is still instructive to discuss how sensitive the model is to the different parameters, as well as environmental parameters, such as carbon content in the material and dose rate, which will be done is this section.

6.2.1 Parametric studies

The threshold parameters (N_{th}^{low} and N_{th}^{high}) have similar functions at both low ($\sim$340 K) and high ($\sim$560 K) irradiation temperature, as they give the size dependency of the SIA cluster trapping energy. However, at low temperature, the N_{th}^{low} threshold size is coupled to the probability for a C-V cluster to interact with the edge or the centre of a SIA cluster, which varies with the size of the SIA cluster; whereas at high temperature, the N_{th}^{high} threshold size is instead coupled to the visibility threshold for SIA clusters in TEM. The sensitivity of the threshold parameters was studied for low temperature in Paper **IV** and for high temperature in Paper **V**. The effect of varying the threshold is similar at both low and high temperature, as in both cases a larger threshold gives a lower density of visible SIA clusters (as shown for low temperature in Fig. 6.11), but larger mean sizes, even though the latter effect is not strong at high temperature. The vacancy clusters are not significantly affected by the threshold parameters at either temperature.

The size dependency of traps for SIA clusters was found to be important for both high and low temperature. In Paper **IV**, it was also studied at low temperature if the SIA traps could be substituted by an effective migration energy $M_{eff}^{i}(N^i) = M^i(N^i) + E_{t1}^{i}(N^i)$, where the migration energy of the SIA clusters is increased by the trapping energy. The SIA cluster density did, however, not follow the experimental trend at all with this method (*Cf.* Fig. 6.12) and it is clear that the traps are essential as nucleation points for the growth of large clusters.

For the high temperature model, the other important parameters, beside N_{th}^{high}, were the trapping energy of vacancy clusters, E_t^v, the bias for SIA sinks, Z^i, and the migration energy for invisible SIA clusters, M_s^i. The bias parameter was already discussed in Sec. 6.1.2; its main effect being to delay the growth of visible SIA clusters. The vacancy cluster trapping energy, E_t^v, was found in Paper **V** to

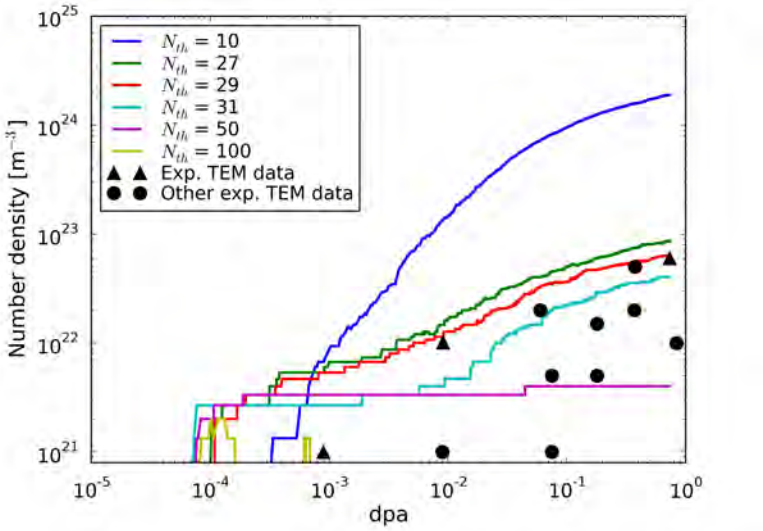

Figure 6.11: Number density of visible SIA versus dpa at 343 K for different values of the threshold parameter, N_{th}^{low}. The reference experimental data are denoted with triangles [44]. Included in the graph are also data from other comparable irradiation experiments in Fe-C (bullets) [42, 72, 74, 78–80]. See [87] for full details. From Paper **IV**.

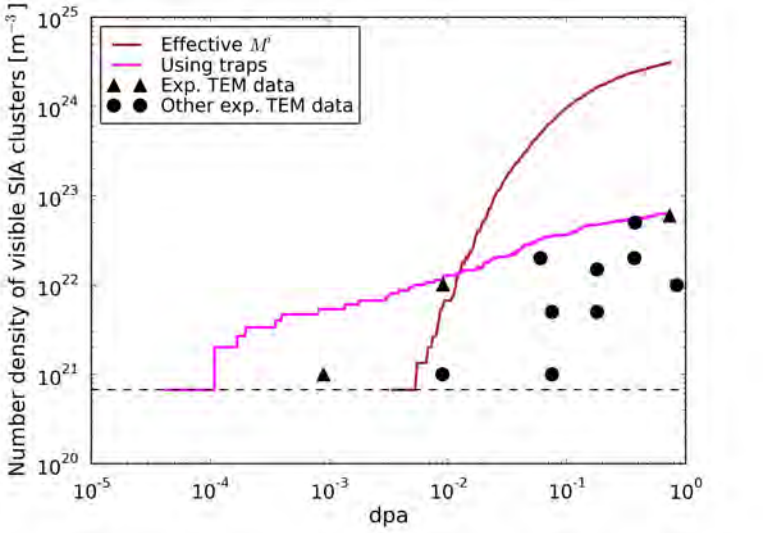

Figure 6.12: Number density of visible SIA versus dpa at 343 K. The dotted line gives the density corresponding to one visible cluster in the box. The reference experimental data are denoted with triangles [44]. Included in the graph are also data from other comparable irradiation experiments in Fe-C (bullets) [42, 72, 74, 78–80]. See [87] for full details. From Paper **IV**.

be much more important at high temperature than at low temperature, where vacancy clusters migrate too slowly to be affected. At high temperature, a higher E_t^v (for clusters $N^v > 6$) increases the cluster densities for both vacancy and visible SIA clusters, as well as the cluster mean sizes. However, the mean size of the large vacancy clusters of sizes observable by SANS ($N^v \geq 50$) decreases with higher E_t^v values, as more strongly trapped vacancy clusters leads to more nucleation points and thereby to slower growth of large vacancy clusters. The best fit was obtained with $E_t^v = 0.4$ eV.

The migration energy for invisible SIA clusters at high temperature, M_s^i, was found to have moderate effect if varied between 0.2 and 0.9 eV, with 0.9 eV being the value of the migration energy attributed to visible $\langle 100 \rangle$ SIA clusters [139]. With 0.1 eV, no growth of visible SIA clusters is observed. A value higher than $M_s^i = 0.1$ eV thus slows down the invisible SIA clusters enough for nucleation and growth of visible SIA clusters to occur. The best fit was found with $M_s^i = 0.2$ eV. The effect on the vacancy clusters is minimal.

6.2.2 Effect of environmental variables

The effect of carbon in the matrix, is studied for both low ($\sim$340 K) and high irradiation ($\sim$560 K) temperature, as reported in Paper **IV** and **V**, respectively. The results for the visible SIA density at low temperature is shown in Fig. 6.13. As the carbon content is represented by the traps, the studies are done by varying the trap concentration. For both low and high temperature, it was found that a higher C concentration leads to increased cluster density, but decreased cluster mean size. The traps work as nucleation points and a larger number of them will slow down the growth of large clusters. The effect is, however, not large. No significant change is observed at low temperature if the carbon concentration is decreased by half, from 100 appm to 50 appm, or increased to 200 appm. Above 50 appm, there appears to be a saturation at low temperature, as not all traps become occupied. For SIA clusters, a significant drop in density is seen only below 5 appm of C content. At high temperature, the effect is similar, with only moderate changes if the C concentration is changed between 50 and 300 appm.

Finally, the effect of the dose rate was studied in Paper **IV** for low temperature. The dose rate was varied from 10^{-11} dpa/s, which corresponds to a typical flux on the RPV wall in a commercial nuclear power plant, to 10^{-3} dpa/s, which corresponds to ion irradiation. The reference experiment at low temperature by Eldrup *et al.* [44, 76] used a high flux of 7×10^{-7} dpa/s, which is typical for test reactors. Since this model is compared to data from such high-flux experiments, it is important to study how much the nanostructure evolution would change in a low flux commercial reactor. The results showed that a lower dose rate gives more time for the clusters to grow by clustering and coalesce before new defects are introduced in the next cascade. Thus, the cluster densities are lower

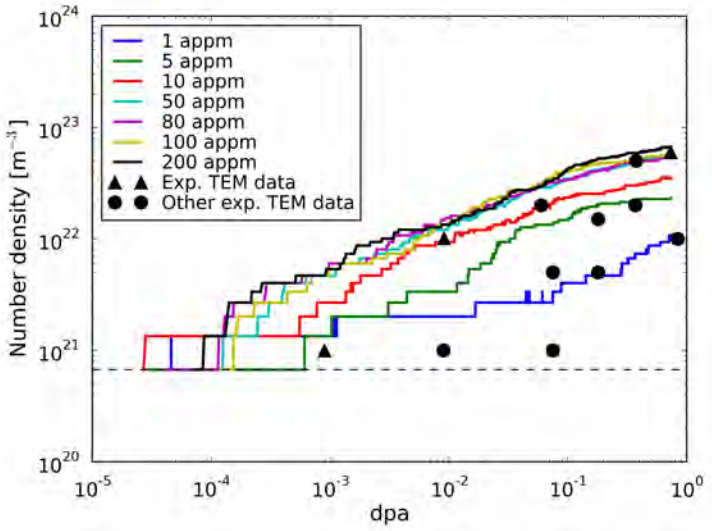

Figure 6.13: Effect of C concentration at 343 K: the visible SIA density versus dpa. The reference experimental data are denoted with triangles [44]. Included in the graph are also data from other comparable irradiation experiments in Fe-C (bullets) [42, 72, 74, 78–80]. See [87] for full details. The dotted line gives the density for one visible cluster in the simulation box. From Paper **IV**.

with lower dose rates, but the mean cluster sizes are larger. The effect is, however, only limited as a change of dose rate by eight orders of magnitude only gives a change of one order of magnitude for both the vacancy and the visible SIA cluster densities (*Cf.* Figs. 6.14 and 6.15, respectively).

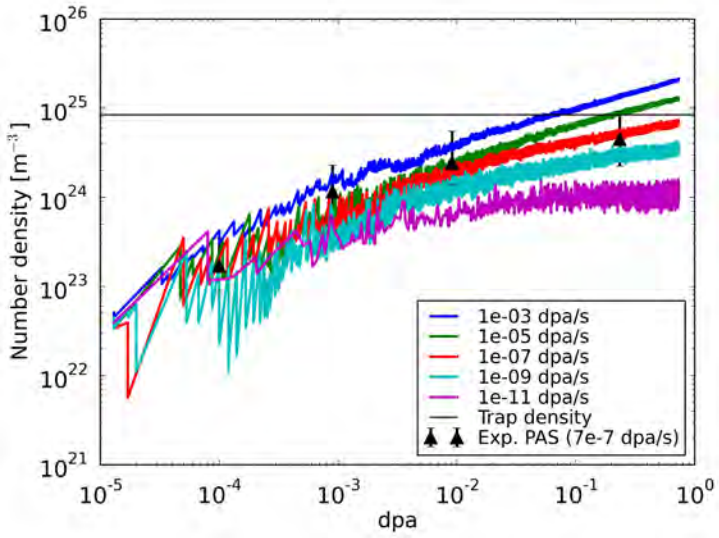

Figure 6.14: Effect of dose on the vacancy density evolution at 343 K. The experimental data are from [76] and correspond to a dose rate of $7 \cdot 10^{-7}$ dpa/s. The black line is the trap density. From Paper **IV**.

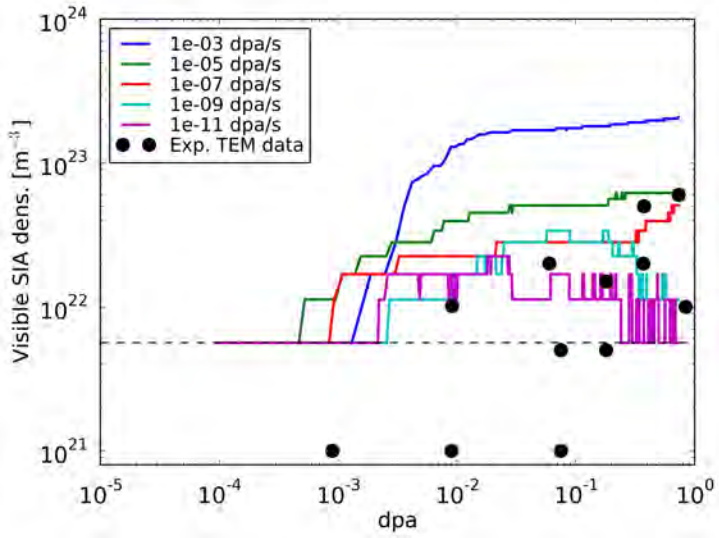

Figure 6.15: Effect of dose rate on the visible SIA cluster density evolution at 343 K. The dotted line gives the density for one visible cluster in the simulation box. The experimental data are from [42, 44, 72, 74, 78–80]. See [87] for full details. From Paper **IV**.

Chapter 7

Summary and perspectives

In this thesis, radiation-induced defects have been studied using Molecular Dynamics (MD) and Object Kinetic Monte Carlo (OKMC) simulation techniques. A model for the radiation-induced nanostructure evolution in Fe-C has been built using OKMC. The model correctly reproduces experimental data in terms of vacancy and SIA cluster densities and mean size evolutions at both low ($<$470 K) and high (560 K) irradiation temperature. The model is also able to reproduce a post-irradiation annealing experiment.

The interaction of interstitial carbon atoms with vacancy clusters and with SIA clusters have been characterized using MD simulations. C atoms alone are found to be not strongly enough bound to SIA clusters to trap them and since SIA clusters are not able to drag C atoms, it is unlikely for several C atoms to trap SIA clusters at low temperature, where C atoms are immobile. However, it has been found that CV_2, C_2V and CV complexes are stable and indeed able to trap SIA clusters at the considered temperatures.

The sink strength of large SIA clusters, represented by toroidal absorbers, and straight dislocations were explored using OKMC and the results were found to be in good agreement with theoretical expressions. The theoretical master curve of the transition of 3D to 1D migrating defects was found to be in excellent agreement with toroidal absorbers and in good agreement with straight dislocations. Together with earlier studies, it can thus be concluded that the master curve is valid for absorbers of all shapes.

The nanostructure evolution model shows the importance of SIA-trapping complexes, such as CV_2, C_2V and C, to reproduce experimental trends. Different complexes are dominant at different temperatures: At low temperature C and CV_2 are the dominant traps and at high temperature, C and C_2V dominate. Above $\sim$680 K, even the CV_2 complex becomes unstable and only C atoms remain

as weak traps. The fact that complexes trap SIA clusters with a binding energy which depends on whether they bind to the edge or the centre of the SIA clusters, as seen in MD studies in Paper **I** and in other studies [140, 141], can be taken into account by having traps with a trapping energy that depends on the size of the trapped SIA cluster. Small clusters are more likely to interact via their edge with C-V complexes, whereas SIA clusters larger than size $\sim$29 are more likely to interact via their centre. The trapping energy also depends on whether the interaction is with $1/2\langle 111\rangle$ SIA clusters, which are dominant at low irradiation temperature, or with $\langle 100\rangle$ SIA clusters which are dominant at high irradiation temperature.

At high irradiation temperature, the model shows that it can not be excluded that small invisible $1/2\langle 111\rangle$ SIA clusters are present beside the $\langle 100\rangle$ SIA clusters that grow large enough to be visible in TEM experiments. The model also shows that one main effect of traps are to function as nucleation points for growth of large SIA clusters, visible by TEM. The effect of traps can not be substituted by an effective high migration energy to slow down the SIA clusters, as the cluster density evolution will in that case not follow the experimental trend. The density of carbon seems, however, not to be crucial for the nanostructural evolution, as the C content can be varied between 50 to 200 appm without any significant change of the cluster evolutions. Significant sensitivity of the C density is only observed at very low densities of 1–5 appm. A limited effect of the dose rate on the cluster evolutions is observed. A lower dose rate gives the defects more time to cluster and coalesce into larger clusters, which in turn will lower the cluster densities.

The model presented in this thesis allows for a deeper understanding of the nanostructure evolution under irradiation in iron alloys. No doubt will the model be refined in the future as our physical understanding of vacancy clusters, C-V complexes and SIA clusters increases. More knowledge about the interaction of C with vacancies and SIA clusters would allow for the substitution of the generic traps in the OKMC model with an explicit description of the C atoms. The effect of explicitly using two families of SIA clusters with the different Burgers vectors, $1/2\langle 111\rangle$ and $\langle 100\rangle$, and taking into account the dynamics between these families, remains an interesting research topic for future research. However, despite the approximations in the model, it provides a good description of the Fe-C system and a good basis for the development of a model of the nanostructure evolution in RPV steels, which would only require the inclusion of solute elements such as Cu, Ni and Mn. As the model is general, it can in principle be adopted and extended to understand the irradiation-induced nanostructure evolution in any steel; also in Generation III and IV reactors, as well as fusion reactors, even though the higher temperatures and the higher dose rates would make the simulations computationally too heavy to be feasible with the CPU-power available today.

Acknowledgement

This thesis project was carried out as a collaboration between the Belgian Nuclear Research Centre, SCK•CEN in Mol, Belgium, and University of Helsinki. I would like to thank the director-general of SCK•CEN, Prof. Eric van Walle, and the head of the Department of Physics, Prof. Juhani Keinonen, for the opportunity to conduct my research. I would also like to thank the current and former head of the Structural Materials expert group, Dr Milan Konstantinovic and Dr Rachid Chaouadi, respectively, and the head of the institute of Nuclear Materials Science, Dr Leo Sannen, as well as the head of the Accelerator Laboratory Division, Prof. Jyrki Räsänen, for providing the facilities and the computational resources to my disposal.

I am most grateful to my mentor at SCK•CEN, the head of the Structural Materials Modelling and Microstructure unit, Dr Lorenzo Malerba, who, despite his chronically busy schedule, always made time to answer my questions and whose knowledge and engagement in nuclear materials science have been a great inspiration for me during my four years in his unit. I would like to thank Dr Dmitry Terentyev for his mentoring especially during my first year; his hard scientific and insightful questions over the years not to be forgotten. I am most grateful to my university promoter, Prof. Kai Nordlund, for all the support and advice he has given me over the years. Many thanks also to Doc. Flyura Djurabekova for her valuable comments on this thesis.

I would like to direct a special thanks to Dr Andrée de Backer for helping me understand and make implementations in the LAKIMOCA code, which was my main tool in my research, and to the creator of LAKIMOCA, Prof. Christophe Domain, and EDF for allowing me to use the code and for the good collaboration. I also want to express my gratitude for the close collaboration and fruitful discussions with Prof. Charlotte Becquart, Dr Napoleón Anento and Prof. Anna Serra.

It has been a pleasure to be part of the modelling team (now the SMM unit). I am very grateful for all the collaborations, all interesting discussions and all pleasant memories that I share with the people that have been part of the team during my four years: Monica, Alexander, Nicholas, Giovanni, Petr, Boris and Amélie. I will neither forget all my other nice colleagues and friends in SCK•CEN and Mol over the years. I especially want to thank Telma, Akira, Hanno, Konstantza, Frédéric, Mariavittoria,

Monika, Erich, Angela, Feyzan, Tamara, Yevhen, Dani and Marlies for your good friendships that have enlightened my days in Mol. You all mean a lot to me. Finally I want to thank my family and friends in Finland for always supporting me.

This work was carried out as part of the PERFORM60 project of the 7th Euratom Framework Programme, partially supported by the European Commission, Grant agreement number FP7-232612.

Helsingfors, 29th October 2013
Ville Jansson

Bibliography

1. C. E. Till and Y. I. Chang, *Plentiful Energy: The Story of the Integral Fast Reactor, the Complex History of a Simple Reactor Technoloogy, with Emphasis on Its Scientific Basis for Non-specialists*. Charles E. Till and Yoon Il Chang, 2011.

2. P. G. Tipping, *Understanding and Mitigating Ageing in Nuclear Power Plants: Materials and Operational Aspects of Plant Life Management (PLiM)*, ch. Introduction to plant life management (PLiM) safety regulation and economics of nuclear power plants. Woodhead Publishing Series in Energy, Woodhead Publishing Limited, 2010.

3. *Nuclear Energy Data 2012*. OECD Publishing, 2012.

4. L. Bernstein, R. K. Pachauri, I. P. on Climate Change, and A. Reisinger, *Climate Change 2007: Synthesis Report*. IPCC, Intergovernmental Panel on Climate Change c/o World Meteorological Organization (WMO), 2008.

5. P. G. Tipping, *Understanding and Mitigating Ageing in Nuclear Power Plants: Materials and Operational Aspects of Plant Life Management (PLiM)*, ch. Key elements and principles of nuclear PLiM. Woodhead Publishing Series in Energy, Woodhead Publishing Limited, 2010.

6. ITER. http://www.iter.org/faq. (Accessed August 2013).

7. PERFORM60. http://perform60.lgi-consulting.eu/. (Accessed August 2013).

8. http://www.nrc.gov/reading-rm/basic-ref/students/animated-bwr.html (Accessed 13th July 2013). United States Nuclear Regulatory Commission. Public Domain.

9. http://www.nrc.gov/reading-rm/basic-ref/students/animated-pwr.html (Accessed 13th July 2013). United States Nuclear Regulatory Commission. Public Domain.

10. M. Brumovsky, *Understanding and Mitigating Ageing in Nuclear Power Plants: Materials and Operational Aspects of Plant Life Management (PLiM)*, ch. Plant life management (PLiM) practices for pressurized light water reactors (PWR). Woodhead Publishing Series in Energy, Woodhead Publishing Limited, 2010.

11. http://www.eia.gov/cneaf/nuclear/page/nuc_reactors/pwr.html (Accessed 13th July 2013). U.S. Energy Information Administration. Public domain.

12. http://www.loc.gov/pictures/resource/hhh.pa1658.photos.135430p (Accessed 13th July 2013). Library of Congress, USA. Public domain.

13. L. Malerba, *Understanding and Mitigating Ageing in Nuclear Power Plants: Materials and Operational Aspects of Plant Life Management (PLiM)*, ch. Multi-scale modelling of irradiation effects in nuclear power plant materials. Woodhead Publishing Series in Energy, Woodhead Publishing Limited, 2010.

14. M. Hernández-Mayoral and M. J. Caturla, *Understanding and Mitigating Ageing in Nuclear Power Plants: Materials and Operational Aspects of Plant Life Management (PLiM)*, ch. Microstructure evolution of irradiated structure materials in nuclear power plants. Woodhead Publishing Series in Energy, Woodhead Publishing Limited, 2010.

15. M. K. Miller, K. F. Russell, M. A. Sokolov, and R. K. Nanstad, "APT characterization of irradiated high nickel RPV steels," *Journal of Nuclear Materials*, vol. 361, no. 2, pp. 248–261, 2007.

16. M. Brumovsky, *Understanding and Mitigating Ageing in Nuclear Power Plants: Materials and Operational Aspects of Plant Life Management (PLiM)*, ch. Irradiation hardening and materials embrittlement in light water reactor(LWR). Woodhead Publishing Series in Energy, Woodhead Publishing Limited, 2010.

17. J. R. Hawthorne, M. A. Sokolov, and W. L. Server, "Exploratory Test of 288 °C Radiation Resistance of Two USSR-Produced Reactor Pressure Vessel Steels," *ASTM SPECIAL TECHNICAL PUBLICATION*, vol. 1366, pp. 16–32, 2000.

18. G. R. Odette and B. D. Wirth, "A computational microscopy study of nanostructural evolution in irradiated pressure vessel steels," *Journal of Nuclear Materials*, vol. 251, pp. 157–171, 1997.

19. W. J. Phythian and C. A. English, "Microstructural evolution in reactor pressure vessel steels," *Journal of Nuclear Materials*, vol. 205, pp. 162–177, 1993.

20. G. R. Odette, "On the ductile to brittle transition in martensitic stainless steels—mechanisms, models and structural implications," *Journal of Nuclear Materials*, vol. 212, pp. 45–51, 1994.

21. F. Seitz, "Radiation effects in solids," *Physics Today*, vol. 5, p. 6, 1952.

22. L. R. Greenwood, "Neutron interactions and atomic recoil spectra," *Journal of Nuclear Materials*, vol. 216, pp. 29–44, 1994.

23. J. A. Brinkman, "On the nature of radiation damage in metals," *Journal of Applied Physics*, vol. 25, no. 8, pp. 961–970, 1954.

24. J. A. Brinkman, "Production of atomic displacements by high-energy particles," *American Journal of Physics*, vol. 24, p. 246, 1956.

25. F. Seitz and J. S. Koehler, "Displacement of atoms during irradiation," *Solid State Physics*, vol. 2, pp. 305–448, 1956.

26. A. K. Seeger, "On the theory of radiation damage and radiation hardening," in *Proceedings of hte Second United Nations International Conference on Peaceful Uses of Atomic Energy*, (Vienna), pp. 250–273, 1958.

27. M. T. Robinson, "Basic physics of radiation damage production," *Journal of Nuclear Materials*, vol. 216, pp. 1–28, 1994.

28. R. S. Averback and T. D. de La Rubia, "Displacement damage in irradiated metals and semiconductors," *Solid State Physics*, vol. 51, pp. 281–402, 1997.

29. R. Bullough, M. H. Wood, R. A. Johnson, and A. N. Orlov, "Theory of microstructural evolution," *Physics of Radiation Effects, Eds. R. A. Johnson and A. N. Orlov, North Holland Physics Publishing, Elsevier Science Publishers BV*, pp. 189–224, 1986.

30. B. L. Eyre and J. R. Matthews, "Technological impact of microstructural evolution during irradiation," *Journal of Nuclear Materials*, vol. 205, pp. 1–15, 1993.

31. L. K. Mansur, "Theory and experimental background on dimensional changes in irradiated alloys," *Journal of Nuclear Materials*, vol. 216, pp. 97–123, 1994.

32. C. A. English, W. J. Phythian, and R. J. McElroy, "Microstructure and modelling of RPV embrittlement," in *MRS Proceedings*, vol. 439, Cambridge Univ Press, 1996.

33. B. N. Singh, S. I. Golubov, H. Trinkaus, A. Serra, Y. N. Osetsky, and A. V. Barashev, "Aspects of microstructure evolution under cascade damage conditions," *Journal of Nuclear Materials*, vol. 251, pp. 107–122, 1997.

34. B. N. Singh, "Impacts of damage production and accumulation on materials performance in irradiation environment," *Journal of Nuclear Materials*, vol. 258, pp. 18–29, 1998.

35. H. Trinkaus, B. N. Singh, and S. I. Golubov, "Progress in modelling the microstructural evolution in metals under cascade damage conditions," *Journal of Nuclear Materials*, vol. 283, pp. 89–98, 2000.

36. J. Gan, G. S. Was, and R. E. Stoller, "Modeling of microstructure evolution in austenitic stainless steels irradiated under light water reactor condition," *Journal of Nuclear Materials*, vol. 299, no. 1, pp. 53–67, 2001.

37. K. Nordlund. http://upload.wikimedia.org/wikipedia/commons/8/88/Cascade_sequence.png (Accessed 13th July 2013). Wikipedia. Public domain.

38. A. V. Barashev, S. I. Golubov, and H. Trinkaus, "Reaction kinetics of glissile interstitial clusters in a crystal containing voids and dislocations," *Philosophical Magazine A*, vol. 81, no. 10, pp. 2515–2532, 2001.

39. M. Lambrecht. PhD thesis, University of Ghent, 2009.

40. M. Lambrecht, E. Meslin, L. Malerba, M. Hernandez-Mayoral, F. Bergner, P. Pareige, B. Radiguet, and A. Almazouzi, "On the correlation between irradiation-induced microstructural features and the hardening of reactor pressure vessel steels," *Journal of Nuclear Materials*, vol. 406, no. 1, pp. 84–89, 2010.

41. E. Meslin, M. Lambrecht, M. Hernández-Mayoral, F. Bergner, L. Malerba, P. Pareige, B. Radiguet, A. Barbu, D. Gómez-Briceño, A. Ulbricht, *et al.*, "Characterization of neutron-irradiated ferritic model alloys and a RPV steel from combined APT, SANS, TEM and PAS analyses," *Journal of Nuclear Materials*, vol. 406, no. 1, pp. 73–83, 2010.

42. B. L. Eyre and A. F. Bartlett, "An electron microscope study of neutron irradiation damage in alpha-iron," *Philosophical Magazine*, vol. 12, no. 116, pp. 261–272, 1965.

43. A. C. Nicol, M. L. Jenkins, and M. A. Kirk, "Matrix damage in iron," in *Materials Research Society Symposium Proceedings*, vol. 650, pp. R1–3, Cambridge Univ Press, 2001.

44. S. J. Zinkle and B. N. Singh, "Microstructure of neutron-irradiated iron before and after tensile deformation," *Journal of Nuclear Materials*, vol. 351, no. 1-3, pp. 269–284, 2006.

45. D. T. Hoelzer and F. Ebrahimi, "Effect of copper and nickel on the neutron irradiation damage in iron alloys," in *MRS Proceedings*, vol. 373, Cambridge Univ Press, 1994.

46. M. Hernández-Mayoral and D. Gómez-Briceño, "Transmission electron microscopy study on neutron irradiated pure iron and RPV model alloys," *Journal of Nuclear Materials*, vol. 399, no. 2–3, pp. 146–153, 2010.

47. Y. N. Osetsky, D. Bacon, A. Serra, B. N. Singh, and S. Golubov, "One-dimensional atomic transport by clusters of self-interstitial atoms in iron and copper," *Philosophical Magazine*, vol. 83, no. 1, pp. 61–91, 2003.

48. D. A. Terentyev, L. Malerba, and M. Hou, "Dimensionality of interstitial cluster motion in bcc-Fe," *Physical Review B*, vol. 75, no. 10, p. 104108, 2007.

49. K. Arakawa, K. Ono, M. Isshiki, K. Mimura, M. Uchikoshi, and H. Mori, "Observation of the one-dimensional diffusion of nanometer-sized dislocation loops," *Science*, vol. 318, no. 5852, p. 956, 2007.

50. Z. Yao, M. Hernández-Mayoral, M. L. Jenkins, and M. A. Kirk, "Heavy-ion irradiations of Fe and Fe–Cr model alloys Part 1: Damage evolution in thin-foils at lower doses," *Philosophical Magazine*, vol. 88, no. 21, pp. 2851–2880, 2008.

51. M. Hernández-Mayoral, Z. Yao, M. L. Jenkins, and M. A. Kirk, "Heavy-ion irradiations of Fe and Fe–Cr model alloys Part 2: Damage evolution in thin-foils at higher doses," *Philosophical Magazine*, vol. 88, no. 21, pp. 2881–2897, 2008.

52. A. J. E. Foreman, W. J. Phythian, and C. A. English, "The molecular dynamics simulation of irradiation damage cascades in copper using a many-body potential," *Philosophical Magazine A*, vol. 66, no. 5, pp. 671–695, 1992.

53. R. E. Stoller, G. R. Odette, and B. D. Wirth, "Primary damage formation in bcc iron," *Journal of Nuclear Materials*, vol. 251, pp. 49–60, 1997.

54. D. J. Bacon, F. Gao, and Y. N. Osetsky, "The primary damage state in fcc, bcc and hcp metals as seen in molecular dynamics simulations," *Journal of Nuclear Materials*, vol. 276, no. 1, pp. 1–12, 2000.

55. J. Marian, B. D. Wirth, and J. M. Perlado, "Mechanism of formation and growth of <100> interstitial loops in ferritic materials," *Physical Review Letters*, vol. 88, no. 25, p. 255507, 2002.

56. H. Xu, R. E. Stoller, Y. N. Osetsky, and D. Terentyev, "Solving the puzzle of <100> interstitial loop formation in bcc iron," *Physical Review Letters*, vol. 110, no. 26, p. 265503, 2013.

57. M. Matijasevic, E. Lucon, and A. Almazouzi, "Behavior of ferritic/martensitic steels after n-irradiation at 200 and 300 °C," *Journal of Nuclear Materials*, vol. 377, no. 1, pp. 101–108, 2008.

58. M. Matijasevic and A. Almazouzi, "Effect of Cr on the mechanical properties and microstructure of Fe–Cr model alloys after n-irradiation," *Journal of Nuclear Materials*, vol. 377, no. 1, pp. 147–154, 2008.

59. C. A. English, W. J. Phythian, J. T. Buswell, J. R. Hawthorne, and P. H. N. Ray, *Effects of Radiation on Materials: 15th International Symposium*, ch. Investigations of Gundremmingen RPV archive material irradiation in light-water and heavy-water reactors. ASTM International, 1992.

60. P. Pareige, R. E. Stoller, K. F. Russell, and M. K. Miller, "Atom probe characterization of the microstructure of nuclear pressure vessel surveillance materials after neutron irradiation and after annealing treatments," *Journal of Nuclear Materials*, vol. 249, no. 2, pp. 165–174, 1997.

61. P. Auger, P. Pareige, S. Welzel, and J. C. Van Duysen, "Synthesis of atom probe experiments on irradiation-induced solute segregation in french ferritic pressure vessel steels," *Journal of Nuclear Materials*, vol. 280, no. 3, pp. 331–344, 2000.

62. R. G. Carter, N. Soneda, K. Dohi, J. M. Hyde, C. A. English, and W. L. Server, "Microstructural characterization of irradiation-induced Cu-enriched clusters in reactor pressure vessel steels," *Journal of Nuclear Materials*, vol. 298, no. 3, pp. 211–224, 2001.

63. M. K. Miller, K. F. Russell, M. A. Sokolov, and R. K. Nanstad, "Atom probe tomography characterization of radiation-sensitive KS-01 weld," *Journal of Nuclear Materials*, vol. 320, no. 3, pp. 177–183, 2003.

64. M. K. Miller and K. F. Russell, "Embrittlement of rpv steels: An atom probe tomography perspective," *Journal of Nuclear Materials*, vol. 371, no. 1, pp. 145–160, 2007.

65. E. Meslin, B. Radiguet, P. Pareige, and A. Barbu, "Kinetic of solute clustering in neutron irradiated ferritic model alloys and a french pressure vessel steel investigated by atom probe tomography," *Journal of Nuclear Materials*, vol. 399, no. 2–3, pp. 137–145, 2010.

66. D. Hull and D. J. Bacon, *Introduction to dislocations*. Butterworth-Heinemann, 2001.

67. B. N. Singh and S. J. Zinkle, "Defect accumulation in pure fcc metals in the transient regime: a review," *Journal of Nuclear Materials*, vol. 206, no. 2, pp. 212–229, 1993.

68. M. Kiritani, "Story of stacking fault tetrahedra," *Materials chemistry and physics*, vol. 50, no. 2, pp. 133–138, 1997.

69. Y. Dai, X. Jia, J. C. Chen, W. F. Sommer, M. Victoria, and G. S. Bauer, "Microstructure of both as-irradiated and deformed 304L stainless steel irradiated with 800 MeV protons," *Journal of Nuclear Materials*, vol. 296, no. 1, pp. 174–182, 2001.

70. R. Schäublin*, Z. Yao, N. Baluc, and M. Victoria, "Irradiation-induced stacking fault tetrahedra in fcc metals," *Philosophical Magazine*, vol. 85, no. 4-7, pp. 769–777, 2005.

71. X. Li and A. Almazouzi, "Deformation and microstructure of neutron irradiated stainless steels with different stacking fault energy," *Journal of Nuclear Materials*, vol. 385, no. 2, pp. 329–333, 2009.

72. J. S. Bryner, "A study of neutron irradiation damage in iron by electron-transmission microscopy," *Acta Metallurgica*, vol. 14, no. 3, pp. 323–336, 1966.

73. B. L. Eyre, "Direct observations of neutron irradiation damage in α-iron," *Philosophical Magazine*, vol. 7, no. 84, pp. 2107–2113, 1962.

74. I. M. Robertson, M. L. Jenkins, and C. A. English, "Low-dose neutron-irradiation damage in [alpha]-iron," *Journal of Nuclear Materials*, vol. 108, pp. 209–221, 1982.

75. F. H. Hammad, M. K. Matta, and K. E. Mohammed, "Eeffect of fast-neutron irradiation on mechanical properties of iron and some iron binary solid solutions," *Journal of Nuclear Materials*, vol. 108, pp. 428–435, 1982.

76. M. Eldrup, B. N. Singh, S. J. Zinkle, T. S. Byun, and K. Farrell, "Dose dependence of defect accumulation in neutron irradiated copper and iron," *Journal of Nuclear Materials*, vol. 307, pp. 912–917, 2002.

77. M. Eldrup and B. N. Singh, "Accumulation of point defects and their complexes in irradiated metals as studied by the use of positron annihilation spectroscopy—a brief review," *Journal of Nuclear Materials*, vol. 323, no. 2, pp. 346–353, 2003.

78. L. L. Horton, J. Bentley, and K. Farrell, "A TEM study of neutron-irradiated iron," *Journal of Nuclear Materials*, vol. 108, pp. 222–233, 1982.

79. B. N. Singh, A. Horsewell, and P. Toft, "Effects of neutron irradiation on microstructure and mechanical properties of pure iron," *Journal of Nuclear Materials*, vol. 271, pp. 97–101, 1999.

80. T. Takeyama, S. Ohnuki, and H. Takahashi *Trans. Japan Steel Iron Inst.*, vol. 21, pp. 326–331, 1981.

81. F. A. Smidt Jr and J. A. Sprague, "Property changes resulting from impurity-defect interactions in iron and pressure vessel steel alloys," *ASTM STP*, vol. 529, pp. 78–91, 1973.

82. M. Matijasevic, W. Van Renterghem, and A. Almazouzi, "Characterization of irradiated single crystals of Fe and Fe-15Cr," *Acta Materialia*, vol. 57, no. 5, pp. 1577–1585, 2009.

83. L. Malerba, E. van Walle, C. Domain, S. Jumel, and J. C. Van Duisen in *Proceedings 10th International Conference on nuclear Engineering (ICONE-10)*, vol. on CD-ROM, (Arlington, VAC, USA), The American Society of Mechanical Engineers, 14–18 April 2002.

84. M. Lambrecht and A. Almazouzi, "Positron annihilation study of neutron irradiated model alloys and of a reactor pressure vessel steel," *Journal of Nuclear Materials*, vol. 385, no. 2, pp. 334–338, 2009.

85. M. Lambrecht, L. Malerba, and A. Almazouzi, "Influence of different chemical elements on irradiation-induced hardening embrittlement of RPV steels," *Journal of Nuclear Materials*, vol. 378, no. 3, pp. 282–290, 2008.

86. F. Bergner, M. Lambrecht, A. Ulbricht, and A. Almazouzi, "Comparative small-angle neutron scattering study of neutron-irradiated Fe, Fe-based alloys and a pressure vessel steel," *Journal of Nuclear Materials*, vol. 399, no. 2–3, pp. 129–136, 2010.

87. L. Malerba, "Experimental reference cases for model validation in fe and fec alloys," tech. rep., Public Deliverable Nr. D1–3.10, FP7/Perform60 Collaborative Project, Grant Agreement Nr. FP7-232612, 2011.

88. Y. Satoh, H. Matsui, and T. Hamaoka, "Effects of impurities on one-dimensional migration of interstitial clusters in iron under electron irradiation," *Physical Review B*, vol. 77, no. 9, p. 094135, 2008.

89. M. L. Jenkins, Z. Yao, M. Hernandez-Mayoral, and M. A. Kirk, "Dynamic observations of heavy-ion damage in Fe and Fe-Cr alloys," *Journal of Nuclear Materials*, vol. 389, no. 2, pp. 197–202, 2009.

90. N. Anento, A. Serra, and Y. N. Osetsky, "Atomistic study of multimechanism diffusion by self-interstitial defects in α-Fe," *Modelling and Simulation in Materials Science and Engineering*, vol. 18, p. 025008, 2010.

91. C.-C. Fu, J. Dalla Torre, F. Willaime, J.-L. Bocquet, and A. Barbu, "Multiscale modelling of defect kinetics in irradiated iron," *Nature materials*, vol. 4, no. 1, pp. 68–74, 2004.

92. C. Domain, C. S. Becquart, and L. Malerba, "Simulation of radiation damage in Fe alloys: an object kinetic Monte Carlo approach," *Journal of Nuclear Materials*, vol. 335, no. 1, pp. 121–145, 2004.

93. M. J. Caturla, N. Soneda, T. Diaz de La Rubia, and M. Fluss, "Kinetic Monte Carlo simulations applied to irradiated materials: The effect of cascade damage in defect nucleation and growth," *Journal of Nuclear Materials*, vol. 351, no. 1–3, pp. 78–87, 2006.

94. M. J. Caturla and C. J. Ortiz, "Effect of self-interstitial cluster migration on helium diffusion in iron," *Journal of Nuclear Materials*, vol. 362, no. 2–3, pp. 141–145, 2007.

95. R. G. Parr and W. Yang, *Density-Functional Theory of Atoms and Molecules*. International Series of Monographs on Chemistry, Oxford University Press, USA, 1989.

96. B. J. Alder and T. E. Wainwright, "Phase transition for a hard sphere system," *The Journal of Chemical Physics*, vol. 27, no. 5, pp. 1208–1209, 1957.

97. A. Rahman, "Correlations in the motion of atoms in liquid argon," *Physical Review*, vol. 136, no. 2A, pp. 405–411, 1964.

98. H. Goldstein, C. Poole, and J. Safko, *Classical Mechanics (International Edition)*. Pearson international edition, Pearson/Addison Wesley, 2002.

99. L. Verlet, “Computer "experiments" on classical fluids. I. Thermodynamical properties of Lennard-Jones molecules,” *Physical Review*, vol. 159, no. 1, p. 98, 1967.

100. C. W. Gear, *Numerical initial value problems in ordinary differential equations*. Prentice Hall PTR, 1971.

101. M. P. Allen and D. J. Tildesley, *Computer simulation of liquids*. Oxford science publications, Clarendon Press, 1994.

102. M. P. Allen and D. J. Tildesley, *Computer simulation of liquids*. Oxford Science Publ, Clarendon Press, 1989.

103. R. A. Johnson, G. J. Dienes, and A. C. Damask, “Calculations of the energy and migration characteristics of carbon and nitrogen in [alpha]-iron and vanadium,” *Acta Metallurgica*, vol. 12, no. 11, pp. 1215–1224, 1964.

104. R. A. Johnson, “Interstitials and Vacancies in α Iron,” *Physical Review A*, vol. 134, no. 5, pp. 1329–1336, 1964.

105. A. J. Bosman, P. E. Brommer, and G. W. Rathenau, “The influence of pressure on the mean time of stay of interstitial nitrogen in iron,” *Physica*, vol. 23, no. 6, pp. 1001–1006, 1957.

106. A. J. Bosman, P. E. Brommer, L. C. H. Eijkelenboom, C. J. Schinkel, and G. W. Rathenau, “The influence of pressure on the mean time of stay of interstitial carbon in iron,” *Physica*, vol. 26, no. 7, pp. 533–538, 1960.

107. J. Bass and D. Lazarus, “Effect of pressure on mobility of interstitial carbon in iron,” *Journal of Physics and Chemistry of Solids*, vol. 23, no. 12, pp. 1820–1821, 1962.

108. M. S. Daw, S. M. Foiles, and M. I. Baskes, “The embedded-atom method: a review of theory and applications,” *Materials Science Reports*, vol. 9, no. 7, pp. 251–310, 1993.

109. C. S. Becquart, J. M. Raulot, G. Bencteux, C. Domain, M. Perez, S. Garruchet, and H. Nguyen, “Atomistic modeling of an Fe system with a small concentration of C,” *Computational Materials Science*, vol. 40, no. 1, pp. 119–129, 2007.

110. D. J. Hepburn and G. J. Ackland, “Metallic-covalent interatomic potential for carbon in iron,” *Physical Review B*, vol. 78, no. 16, p. 165115, 2008.

111. G. J. Ackland, M. I. Mendelev, D. J. Srolovitz, S. Han, and A. V. Barashev, “Development of an interatomic potential for phosphorus impurities in α-iron,” *Journal of Physics: Condensed Matter*, vol. 16, p. S2629, 2004.

112. K. Tapasa, A. V. Barashev, D. J. Bacon, and Y. N. Osetsky, “Computer simulation of the interaction of carbon atoms with self-interstitial clusters in [alpha]-iron,” *Journal of Nuclear Materials*, vol. 361, no. 1, pp. 52–61, 2007.

113. K. Tapasa, A. V. Barashev, D. J. Bacon, and Y. N. Osetsky, "Computer simulation of carbon diffusion and vacancy-carbon interaction in [alpha]-iron," *Acta Materialia*, vol. 55, no. 1, pp. 1–11, 2007.

114. K. Tapasa, Y. N. Osetsky, and D. J. Bacon, "Computer simulation of interaction of an edge dislocation with a carbon interstitial in α-iron and effects on glide," *Acta Materialia*, vol. 55, no. 1, pp. 93–104, 2007.

115. C. Domain, C. S. Becquart, and J. Foct, "Ab initio study of foreign interstitial atom (C, N) interactions with intrinsic point defects in α-Fe," *Physical Review B*, vol. 69, no. 14, p. 144112, 2004.

116. N. Metropolis and S. Ulam, "The monte carlo method," *Journal of the American statistical association*, vol. 44, no. 247, pp. 335–341, 1949.

117. N. Metropolis, A. Rosenbluth, M. N. Rosenbluth, A. H. Teller, and E. Teller, "Equation of state calculations by fast computing machines," *The journal of chemical physics*, vol. 21, no. 6, p. 1087, 1953.

118. S. K. Theiss, M. J. Caturla, M. D. Johnson, J. Zhu, T. Lenosky, B. Sadigh, and T. Diaz de la Rubia, "Atomic scale models of ion implantation and dopant diffusion in silicon," *Thin Solid Films*, vol. 365, no. 2, pp. 219–230, 2000.

119. K. A. Fichthorn and W. H. Weinberg, "Theoretical foundations of dynamical monte carlo simulations," *The Journal of Chemical Physics*, vol. 95, p. 1090, 1991.

120. A. B. Bortz, M. H. Kalos, and J. L. Lebowitz, "A new algorithm for Monte Carlo simulation of Ising spin systems," *Journal of Computational Physics*, vol. 17, no. 1, pp. 10–18, 1975.

121. W. M. Young and E. W. Elcock, "Monte Carlo studies of vacancy migration in binary ordered alloys: I," *Proceedings of the Physical Society*, vol. 89, p. 735, 1966.

122. R. E. Stoller, "Point defect survival and clustering fractions obtained from molecular dynamics simulations of high energy cascades," *Journal of Nuclear Materials*, vol. 233, pp. 999–1003, 1996.

123. R. E. Stoller and A. F. Calder, "Statistical analysis of a library of molecular dynamics cascade simulations in iron at 100 k," *Journal of Nuclear Materials*, vol. 283, pp. 746–752, 2000.

124. R. E. Stoller, "Evaluation of neutron energy spectrum effects and RPV thru-wall attenuation based on molecular dynamics cascade simulations," *Nuclear Engineering and Design*, vol. 195, no. 2, pp. 129–136, 2000.

125. R. E. Stoller and S. G. Guiriec, "Secondary factors influencing cascade damage formation," *Journal of Nuclear Materials*, vol. 329, pp. 1238–1242, 2004.

126. R. E. Stoller, "The role of cascade energy and temperature in primary defect formation in iron," *Journal of Nuclear Materials*, vol. 276, no. 1-3, pp. 22–32, 2000.

127. M. W. Finnis and J. E. Sinclair, "A simple empirical N-body potential for transition metals," *Philosophical Magazine A*, vol. 50, no. 1, pp. 45–55, 1984.

128. M. T. Norgett *et al.*, "A proposed method of calculating displacement dose rates," *Nuclear Engineering and Design*, vol. 33, no. 1, pp. 50–54, 1975.

129. L. Malerba, C. S. Becquart, and C. Domain, "Object kinetic Monte Carlo study of sink strengths," *Journal of Nuclear Materials*, vol. 360, no. 2, pp. 159–169, 2007.

130. Y. N. Osetsky, "Atomistic study of diffusional mass transport in metals," in *Defect and Diffusion Forum*, vol. 188, pp. 71–92, Trans Tech Publ, 2001.

131. M. I. Mendelev, S. Han, D. J. Srolovitz, G. J. Ackland, D. Y. Sun, and M. Asta, "Development of new interatomic potentials appropriate for crystalline and liquid iron," *Philosophical magazine*, vol. 83, no. 35, pp. 3977–3994, 2003.

132. M. I. Pascuet, N. Castin, C. S. Becquart, and L. Malerba, "Stability and mobility of Cu-vacancy clusters in Fe-Cu alloys: A computational study based on the use of artificial neural networks for energy barrier calculations," *Journal of Nuclear Materials*, vol. 412, pp. 106–115, 2011.

133. N. Castin, M. I. Pascuet, and L. Malerba, "Mobility and stability of large vacancy and vacancy–copper clusters in iron: An atomistic kinetic Monte Carlo study," *Journal of Nuclear Materials*, vol. 429, no. 1, pp. 315–324, 2012.

134. F. A. Nichols, "Kinetics of diffusional motion of pores in solids: A review," *Journal of Nuclear Materials*, vol. 30, no. 1–2, pp. 143–165, 1969.

135. S. I. Golubov, R. E. Stoller, S. J. Zinkle, and A. M. Ovcharenko, "Kinetics of coarsening of helium bubbles during implantation and post-implantation annealing," *Journal of Nuclear Materials*, vol. 361, no. 2–3, pp. 149–159, 2007.

136. S. Takaki, J. Fuss, H. Kuglers, U. Dedek, and H. Schultz, "The resistivity recovery of high purity and carbon doped iron following low temperature electron irradiation," *Radiation Effects and Defects in Solids*, vol. 79, no. 1, pp. 87–122, 1983.

137. C. C. Fu, F. Willaime, and P. Ordejón, "Stability and mobility of mono- and di-interstitials in α-Fe," *Physical Review Letters*, vol. 92, no. 17, p. 175503, 2004.

138. D. A. Terentyev, T. P. C. Klaver, P. Olsson, M. C. Marinica, F. Willaime, C. Domain, and L. Malerba, "Self-trapped interstitial-type defects in iron," *Physical Review Letters*, vol. 100, no. 14, p. 145503, 2008.

139. Y. N. Osetsky. Private communication, 2013.

140. N. Anento and A. Serra, "Carbon–vacancy complexes as traps for self-interstitial clusters in Fe–C alloys," *Journal of Nuclear Materials*, vol. 440, no. 1–3, pp. 236–242, 2013.

141. N. Anento and A. Serra. Private communication, 2013.

142. C. S. Becquart and C. Domain, "PERFORM60 report," April 2011.

143. A. D. Brailsford and R. Bullough, "The theory of sink strengths," *Philosophical Transactions of the Royal Society of London. Series A, Mathematical and Physical Sciences*, vol. 302, no. 1465, pp. 87–137, 1981.

144. F. A. Nichols, "On the estimation of sink-absorption terms in reaction-rate-theory analysis of radiation damage," *Journal of Nuclear Materials*, vol. 75, no. 1, pp. 32–41, 1978.

145. R. E. Stoller, S. I. Golubov, C. Domain, and C. S. Becquart, "Mean field rate theory and object kinetic Monte Carlo: a comparison of kinetic models," *Journal of Nuclear Materials*, vol. 382, no. 2, pp. 77–90, 2008.

146. C. J. Ortiz and M. J. Caturla, "Simulation of defect evolution in irradiated materials: Role of intracascade clustering and correlated recombination," *Physical Review B*, vol. 75, no. 18, p. 184101, 2007.

147. C. J. Ortiz and M. J. Caturla, "Cascade damage evolution: rate theory versus kinetic Monte Carlo simulations," *Journal of Computer-Aided Materials Design*, vol. 14, no. 1, pp. 171–181, 2007.

148. H. Wiedersich, "On the theory of void formation during irradiation," *Radiation Effects*, vol. 12, no. 1–2, pp. 111–125, 1972.

149. H. Trinkaus, B. N. Singh, and S. I. Golubov, "Reaction Kinetics of SIA Clusters and Damage Accumulation in Metals under Cascade Irradiation: Impact of Impurities," in *Proceedings of Second International Conference on Multiscale Materials Modeling*, 2004.

150. G. G. Lee, J. Kwon, and D. S. Kim, "A kinetic Monte Carlo approach for the analysis of trapping effect on the defect accumulation in neutron-irradiated Fe," *Nuclear Instruments and Methods in Physics Research Section B*, vol. 267, no. 18, pp. 3214–3217, 2009.